

Progress toward Characterization of the Atmospheric Boundary Layer over Northern Alabama Using Observations by a Vertically Pointing, S-Band Profiling Radar during VORTEX-Southeast

ROBIN L. TANAMACHI

Department of Earth, Atmospheric, and Planetary Sciences, Purdue University, West Lafayette, Indiana

STEPHEN J. FRASIER AND JOSEPH WALDINGER

Microwave Remote Sensing Laboratory, University of Massachusetts Amherst, Amherst, Massachusetts

ALLISON LAFLEUR

Department of Earth, Atmospheric, and Planetary Sciences, Purdue University, West Lafayette, Indiana

DAVID D. TURNER

NOAA/OAR/ESRL Global Systems Division, Boulder, Colorado

FRANCESC ROCADENBOSCH

CommSensLab, Department of Signal Theory and Communications, Universitat Politècnica de Catalunya, Barcelona, Spain

(Manuscript received 30 November 2018, in final form 23 July 2019)


ABSTRACT

During spring 2016 and spring 2017, a vertically pointing, S-band Frequency Modulated Continuous Wave radar (UMass FMCW) was deployed in northern Alabama under the auspices of the Verification of the Origins of Rotation in Tornadoes Experiment (VORTEX)-Southeast. In total, ~14 weeks of data were collected, in conditions ranging from quiescent clear skies to severe thunderstorms. The principal objective of these deployments was to characterize the boundary layer evolution near the VORTEX-Southeast domain. In this paper, we describe intermediate results in service of this objective. Specifically, we describe updates to the UMass FMCW system, document its deployments for VORTEX-Southeast, and apply four automated algorithms: 1) a dealiasing algorithm to the Doppler velocities, 2) a fuzzy logic scatterer classification scheme to separate precipitation from nonprecipitation observations, 3) a brightband/melting-layer identification algorithm for stratiform precipitation, and 4) an extended Kalman filter–based convective boundary layer depth (mixing height) measurement algorithm for nonprecipitation observations. Results from the latter two applications are qualitatively verified against retrieved soundings from a collocated thermodynamic profiling system.

1. Introduction

The spatiotemporal variability of the atmospheric boundary layer (BL) regulates atmosphere's ability to generate and sustain severe thunderstorms. The

atmospheric BL is defined by [Stull \(1988\)](#) as “that part of the troposphere that is influenced by the presence of the earth's surface, and responds to surface forcings with a time scale of about an hour or less.” BL evolution poses significant challenges for numerical weather prediction (NWP) because both its vertical and horizontal inhomogeneities are unresolved by most operational NWP models (e.g., [Stensrud 2007](#)). Additionally, the BL is difficult to observe over large horizontal areas via remote sensing instruments; scanning ground-based sensors (e.g., [Melnikov et al. 2013](#)) are inhibited by

 Denotes content that is immediately available upon publication as open access.

Corresponding author: Robin L. Tanamachi, rtanamachi@purdue.edu

DOI: 10.1175/JTECH-D-18-0224.1

© 2019 American Meteorological Society. For information regarding reuse of this content and general copyright information, consult the [AMS Copyright Policy](#) (www.ametsoc.org/PUBSReuseLicenses).

terrain blockage, while spaceborne sensors find upwelling radiation from the BL mostly overwhelmed by radiation from the free atmosphere (i.e., the layer above the BL). There are several ground-based technologies such as multichannel microwave radiometers (e.g., Rose et al. 2005), infrared spectrometers (Knuteson et al. 2004a,b), and water vapor lidars (e.g., Spuler et al. 2015) that are able to provide temperature and/or water vapor profiles through the BL at high temporal resolution. The review paper by Wulfmeyer et al. (2015) provides an overview of these different methods. However, these instruments all have strengths and weaknesses, and in particular are often compromised during precipitating conditions. Thus, complementing these technologies with a ground-based vertically pointing radar can reveal additional details about the evolution and character of the BL.

While BL profiling is commonly accomplished using UHF profilers (Angevine et al. 1994), the use of S-band (~10-cm wavelength) radars for BL profiling is also generally accepted practice (Gossard 1990; Wilczak et al. 1995). Like the UHF band, the S band straddles the Bragg regime (which dominates in clear air at wavelengths shorter than 10 cm) and the Rayleigh regime (which dominates in most classes of precipitation at wavelengths longer than 10 cm). Bragg scatter becomes increasingly important at wavelengths longer than 10 cm, but is still dominated by Rayleigh scatter in both UHF and S bands when precipitation is present. Therefore, S-band radar is useful both for clear-air BL studies and precipitation studies, a property that led to its adoption in the U.S. National Weather Service Radar—1988 Doppler (WSR-88D; Crum and Alberty 1993). While the WSR-88D was primarily designed for monitoring precipitation, its S-band radar observations can be used for real-time monitoring of the convective boundary layer (CBL), where insect concentrations and Bragg scatter illuminate the horizontal structures within the CBL (Gossard and Strauch 1983; Gossard 1990; Eaton et al. 1995; Melnikov and Zrnić 2017; Richardson et al. 2017). WSR-88D observations of the BL, however, are limited to within approximately 80 km of the WSR-88D by its volume coverage pattern (Heinselman et al. 2009; Melnikov et al. 2011, 2013; Richardson et al. 2017). For reference, in clear air mode, the WSR-88D currently scans nine elevation angles ranging from 0.5° to 6.4° in a step-spiral pattern (VCP 35; Banghoff et al. 2018), and has range and azimuthal resolutions of 250 m and 1.0°, respectively.

From radar observations of precipitation in the BL, there is also information to be gained regarding precipitation microphysical processes. Falling precipitation undergoes a multitude of changes owing to freezing,

melting, evaporation, collision, coalescence, and other microphysical processes (e.g., Fabry et al. 1992; Fabry and Zawadzki 1995; White et al. 2002; Ikeda et al. 2005; Pruppacher and Klett 2010; Emory et al. 2014; Giangrande et al. 2016). Vertical cross sections (reconstructed RHI plots) of WSR-88D observations can be generated from WSR-88D volume coverage patterns (e.g., Brown et al. 2005), but this evolution is captured at relatively coarse temporal (~5 min) and vertical (~100–1000 m) intervals—the latter increases with distance from the radar. Analytical techniques such as quasi-vertical profiling (QVP; Ryzhkov et al. 2016) can be used to generate time series of reflectivity BL profiles with higher vertical resolution (~100 m at altitudes less than 2 km above radar level) than the reconstructed RHIs. However, the QVP technique does not alleviate the temporal coarseness of the WSR-88D volumes, nor does it produce estimates of vertical velocity over the radar site.

In this study, we describe a scatterer identification scheme for data collected in northern Alabama over several weeks by a vertically pointing, S-band radar with high temporal (~16 s) and vertical (~5 m) resolution. This categorization scheme will enable us to isolate specific types of echoes within the overall dataset for further study. After first dealiasing the observations and separating the observations into hydrometeor and hydrometeor-free categories, we further divide the hydrometeor category into convective and stratiform subcategories, and apply a modified operational brightband identification (BBID) algorithm (Zhang et al. 2008) to delineate the melting layer (ML). Within the hydrometeor-free category, we use an extended Kalman filter–based method (Lange et al. 2015) to objectively identify the CBL depth in a pretornadic environment.

A comprehensive review of the use of vertically pointing radar in hydrometeor-free BL studies is provided by Gossard (1990). In summary, vertically pointing radars have revealed multiple finescale layers within the CBL, often with differing refractive properties and stability. During the morning transition following sunrise, the CBL generally increases in depth with time as buoyant thermals rise away from Earth's surface, eroding the capping inversion and residual layer from below via turbulent mixing at the BL/free atmosphere interface (also called the entrainment zone; Stull 1988; Fig. 1a). The success of individual thermal plumes in penetrating the top of the CBL depends on the thermodynamic properties of the plume, the properties of the internal CBL structure (which can be detected using some types of vertically pointing radars and profilers; e.g., Fig. 1b), and the strength of the capping inversion. Depending on the stability of the overlying

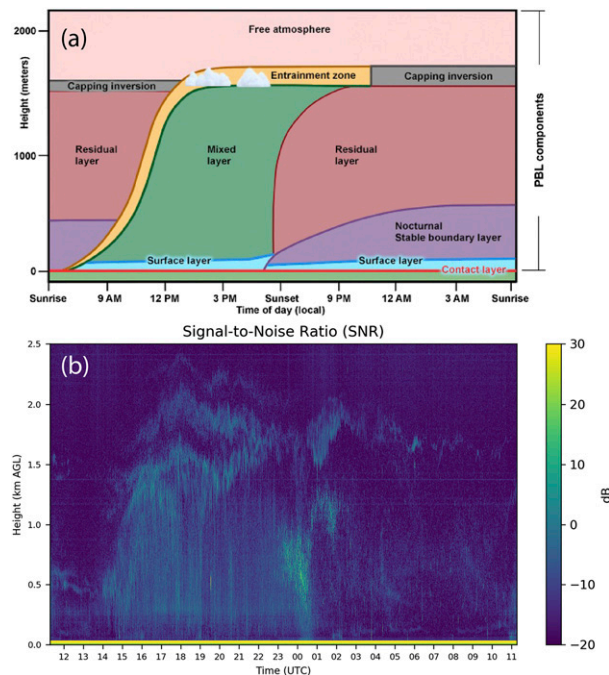


FIG. 1. (a) Conceptual model of the diurnal evolution of the continental CBL (annotated here as the “Mixed layer”) in the absence of precipitation. The image is provided through the courtesy of Kluwer Academic Publishers and is based on a figure from Stull (1988). (b) SNR measurements from the vertically pointing, S-band UMass FMCW from 1117 UTC 10 Apr to 1116 UTC 11 Apr 2017 at Scottsboro. Start and end times match local sunrise.

free atmosphere, penetration of the capping inversion may initiate severe convection. Continued ingestion of unstable BL air by a convective storm in a favorable thermodynamic environment can strengthen and sustain a severe storm’s updraft, leading to increased potential for vorticity stretching, mesocyclogenesis, and ultimately tornadogenesis within the storm (Weisman and Klemp 1982; Rasmussen and Blanchard 1998; Atkins et al. 1999; Markowski and Richardson 2009; Nowotarski et al. 2011).

The Verification of the Origin of Rotation in Tornadoes Experiment–Southeast (hereinafter VORTEX-SE) experiment was instigated to intensively investigate tornadoes, their environments, and their societal impact in the southeastern United States (Koch 2016; Rasmussen and Koch 2016). Among the science objectives outlined for this project was characterization of BL evolution and precipitation microphysical processes over the VORTEX-SE domain (Fig. 2a). In this paper, we report on data collection in northern Alabama by a vertically pointing, S-band, BL profiling radar during VORTEX-SE in 2016 and 2017 in service of this objective, and some data quality control and

enhancement techniques applied to these data. The purposes of this paper are 1) to update the description of the radar system, 2) to document its 2016 and 2017 VORTEX-SE deployments in northern Alabama, 3) to describe quality control procedures applied to these data, 4) to describe a precipitation/nonprecipitation classification scheme developed using the VORTEX-SE data, and 5) to provide an example application for each classification. Specifically, we will demonstrate 5a) a melting-layer identification for the precipitation observations and 5b) an extended Kalman filter–based CBL/mixing height detection algorithm applied to the nonprecipitation observations. This study should be considered to be a progress report of a larger effort toward a more comprehensive characterization of the CBL over the VORTEX-SE domain.

2. The UMass FMCW radar

a. Instrument description

The University of Massachusetts Frequency Modulated Continuous Wave radar (hereinafter UMass FMCW) was constructed at the Microwave Remote Sensing Laboratory (Eaton et al. 1995; İnce et al. 2000, 2003). UMass FMCW is a vertically pointing, S-band, pulse compression, single-polarized, BL profiling radar with exceptionally fine range-gate spacing (5.0 m) and temporal resolution (as fine as 1 s; Table 1). While UMass FMCW is mounted on a truck for mobility (Fig. 2), it is not designed for rapid deployment. Instead, UMass FMCW is typically deployed at a fixed site for a period of weeks or months, operates off line (A/C) power, and automatically collects a continuous series of observations of the BL directly above the instrument. Prior to VORTEX-SE, UMass FMCW was deployed during other BL observation programs such as the 1999 Cooperative Atmosphere–Surface Exchange Study (CASES-99; İnce et al. 2000; Poulos et al. 2002; İnce et al. 2003) and the International H₂O Project (Weckwerth et al. 2004) to infer BL stratification (Frasier et al. 2002; Demoz et al. 2006; Lange et al. 2015) and insect concentration (Contreras and Frasier 2008).

During VORTEX-SE, UMass FMCW operated as follows: over a 1.34-s interval, 256 frequency modulated sweeps were collected to produce a Doppler spectrum. Fourteen such spectra, spanning a 16.1-s interval, were then averaged and moments were calculated from the averaged spectra. Reflectivity ($\eta; \text{m}^{-1}$) was estimated from system signal-to-noise ratio (SNR) using the radar equation [e.g., Doviak and Zrnić 1993, their Eq. (4.16)] and nominal system parameters (Table 1). Linear radar reflectivity factor ($z; \text{mm}^6 \text{m}^{-3}$) was calculated from η ,

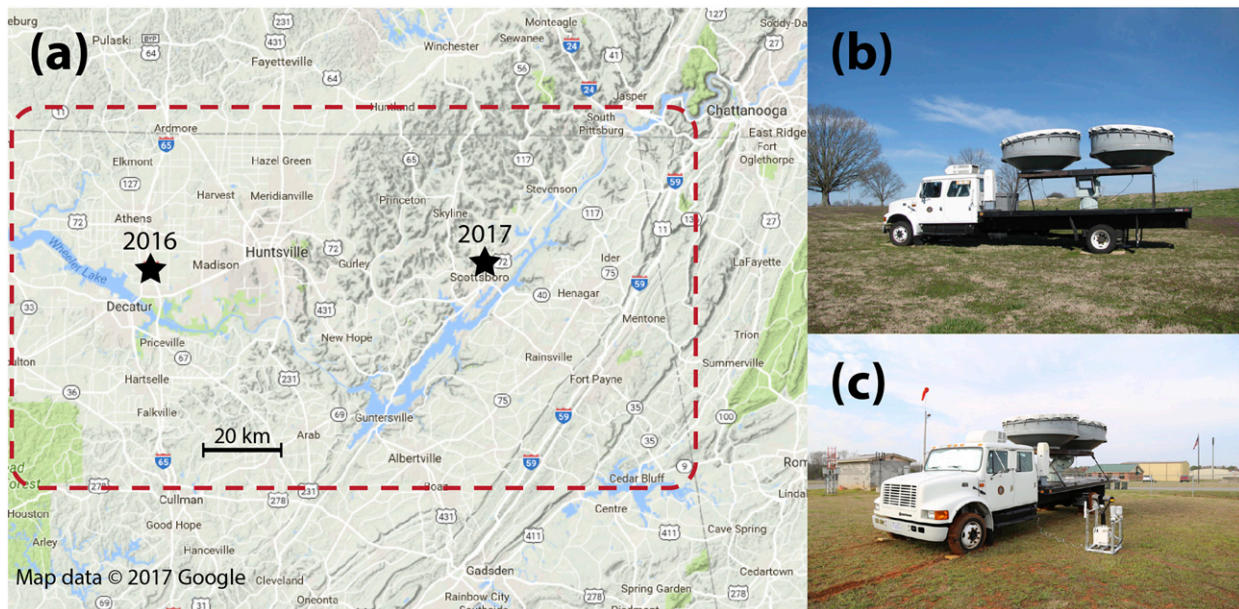


FIG. 2. (a) Approximate boundary (red dashed line) of the VORTEX-SE domain, and the deployment sites (starred) for UMass FMCW in northern Alabama during the 2016 and 2017 field campaigns. (b) The UMass FMCW deployed at the Tennessee Valley Research and Extension Center near Belle Mina in 2016. (c) The UMass FMCW deployed at the Scottsboro municipal airport in 2017. A collocated Portable In Situ Precipitation Station (Dawson et al. 2017) sits beside the truck.

and radial (vertical) Doppler velocity w and spectrum width σ_w were calculated from the Doppler spectra. Examples of these moments, plotted in time–height space, are shown in Figs. 3a–d. In a change from previous field campaigns, the Doppler spectra were also recorded for VORTEX-SE. During CASES-99 (Poulos et al. 2002) and IHOP_2002 (Weckwerth et al. 2004), a lower pulse repetition frequency (20 Hz) was used, and the resulting Doppler spectra (confined to a Nyquist interval of $\pm 0.5 \text{ m s}^{-1}$) were not retained.

b. Deployment during VORTEX-SE

For the 2016 VORTEX-SE field campaign, UMass FMCW was deployed at the Tennessee Valley Research and Extension Center (operated by Auburn University) near Belle Mina, Alabama (Figs. 2a,b), (latitude: 34.6904°N , longitude: 86.8815°W) approximately 22 km west-southwest of Huntsville, Alabama. This site was selected because of its relative freedom from nearby clutter targets, its “upstream” location from the Huntsville domain, and collocation with other VORTEX-SE meteorological measurement systems, including the Collaborative Lower Atmospheric Mobile Profiling System (CLAMPS; Wagner et al. 2019) and NOAA supplemental upper-air measurements (Lee et al. 2018, 2019). UMass FMCW operated almost continuously from 1 March to 30 April 2016 (Frasier and Waldinger 2016). Only a handful of observation discontinuities, and only one more than

24 h in length, occurred during this period (Fig. 4). Most of these data gaps resulted from temporary power or communications outages or from overheating of the UMass FMCW signal processing computer when the external air temperature exceeded 27°C . In the latter case, automated observations typically resumed once the external air cooled.

During the 2017 VORTEX-SE field campaign, UMass FMCW and CLAMPS were instead deployed at the Scottsboro, Alabama, municipal airport (latitude:

TABLE 1. Selected parameters of the UMass FMCW radar system as configured for VORTEX-Southeast.

Parameter	Value
Frequency	2.92 GHz
Bandwidth	30 MHz
Sweep rate (PRF)	190.735 Hz (2016) 287.224 Hz (2017)
Amplifier type	Traveling wave tube (2016) Solid state GaN (2017)
Transmitted power (continuous)	250 W
Antenna gain	34 dB
Compression gain	50.2 dB
Noise level	-97.4 dBm
3-dB beamwidth	3.5°
Max unambiguous range	5.0 km
Max unambiguous velocity	$\pm 4.9 \text{ m s}^{-1}$ (2016) $\pm 7.3 \text{ m s}^{-1}$ (2017)
Sampling period	1.34 s
Averaging period	16.1 s
Range resolution	5.0 m

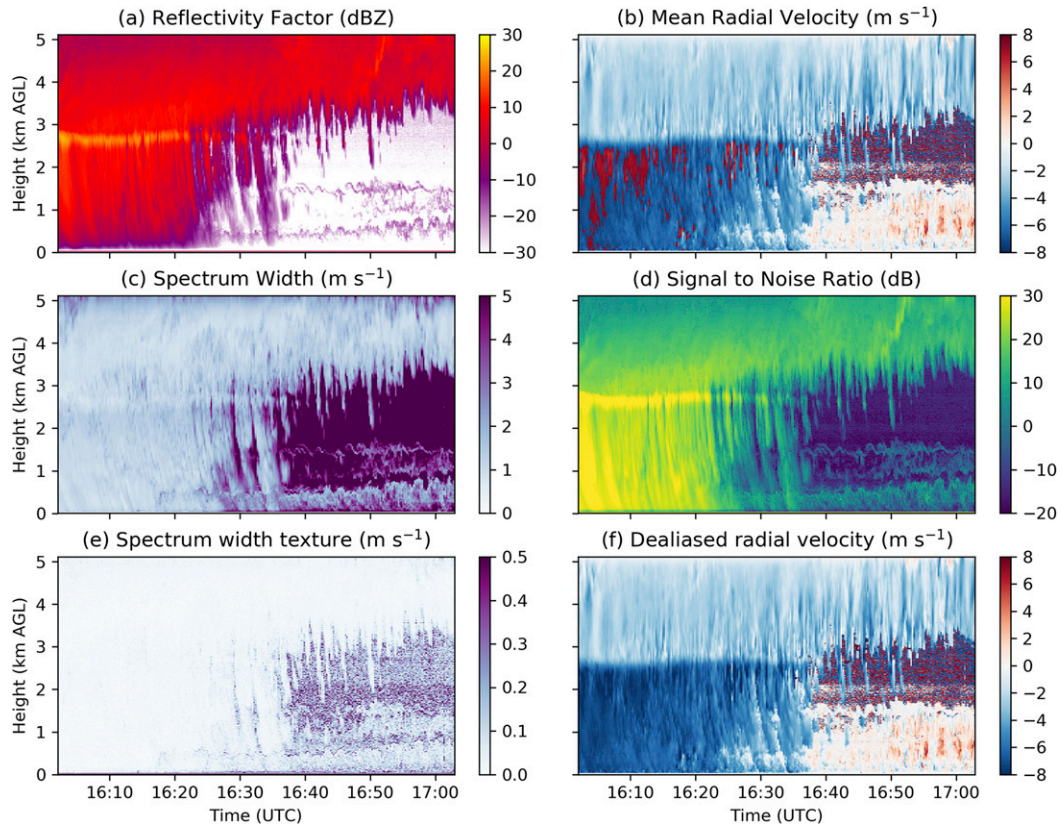


FIG. 3. UMass FMCW observations of (a) reflectivity factor (dBZ), (b) raw Doppler radial velocity (m s^{-1}), (c) spectrum width (m s^{-1}), and (d) SNR (dB) from 1600 to 1700 UTC 3 Apr 2017 above the Scottsboro airport. The end of a stratiform precipitation event with an evident melting layer (around 2.8 km AGL) can be seen, following which at least two elevated, turbulent layers (at approximately 1.0 and 1.5 km AGL) are visible in the hydrometeor-free air. Derived quantities (e) spectrum width texture (m s^{-1}) and (f) dealiased Doppler radial velocity (m s^{-1}) are also shown.

34.6872°N, longitude: 86.0050°W; Figs. 2a,c). This site was selected to align with the objectives of VORTEX-SE pertaining to terrain influences on tornadogenesis. Scottsboro is located west (nominally upstream) of the southern Cumberland terrain range (known locally as Sand Mountain), where a regional maximum in tornadogenesis events has been documented (Lyza and Knupp 2018). UMass FMCW operated at Scottsboro from 10 March to 1 May 2017, with only a few gaps in data coverage (Frasier et al. 2017) (Fig. 5). The most significant gap (12–15 March 2017) resulted from an extended connectivity outage. In total, UMass FMCW observations spanning ~ 108 days were collected in northern Alabama over the two years of VORTEX-SE field operations.

c. Observation quality control

The UMass FMCW dataset included the Doppler spectra and four primary variables: logarithmic reflectivity factor Z (dBZ), SNR, w , and σ_w (Figs. 3a–d,

respectively). Some data quality issues and artifacts were addressed at the spectrum level, and others were addressed in the moments data.

First, the 2016 Doppler spectra contained spurs resulting from interference from high-voltage switching power supplies in the traveling wave tube (TWT) amplifier (Waldinger et al. 2017; Waldinger 2018). These spurs manifest as spurious peaks in the Doppler spectra (e.g., Fig. 6a). A median filtering method was used to ameliorate most of these spurs (e.g., Fig. 6b), but some strong spurs persisted and were visible in the moments data as false echoes appearing a constant height in each variable (e.g., Fig. 7). In the presence of strong scattering, it was impossible to separate the spurs from the backscattered signal. While the spurs generally appeared at the same range gate, they drifted in frequency over time, making the application of a notch filter inadvisable. At the time of this writing, the authors are exploring image processing techniques to more effectively remove these spurs prior to moment

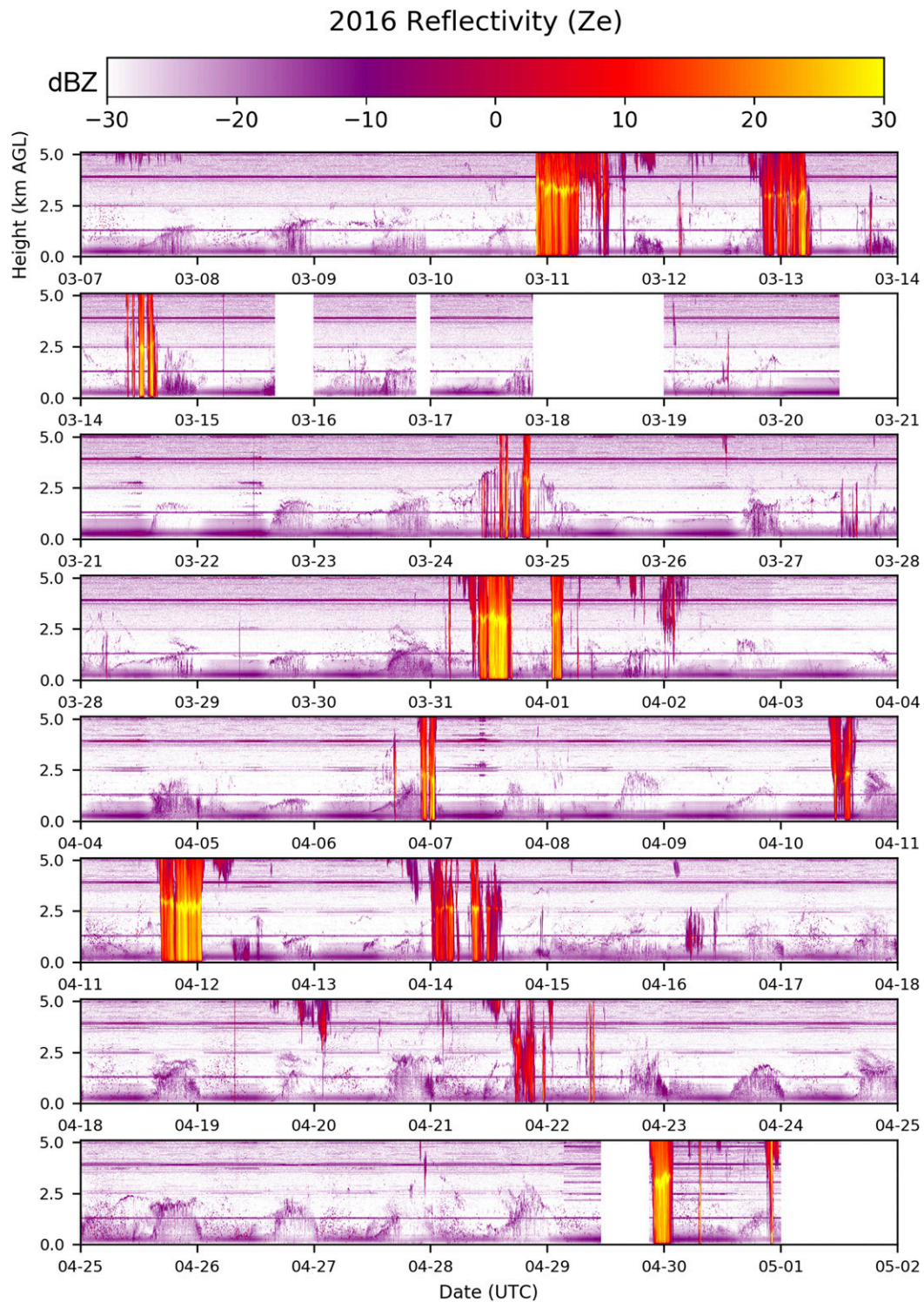


FIG. 4. UMass FMCW reflectivity (dBZ) observed during the 2016 VORTEX-SE field observation campaign.

calculation (Rocadenbosch et al. 2018). For the moment, gates consistently affected by these spurs have simply been flagged for discrimination in later study. Another phenomenon known as “horizon glow”—artificially

enhanced echoes within the lowest 700 m (Fig. 4)—resulted from low-frequency receiver saturation in the TWT at short ranges (i.e., low altitudes). The receiver saturation appears as a relatively continuous echo that

2017 Reflectivity (Ze)

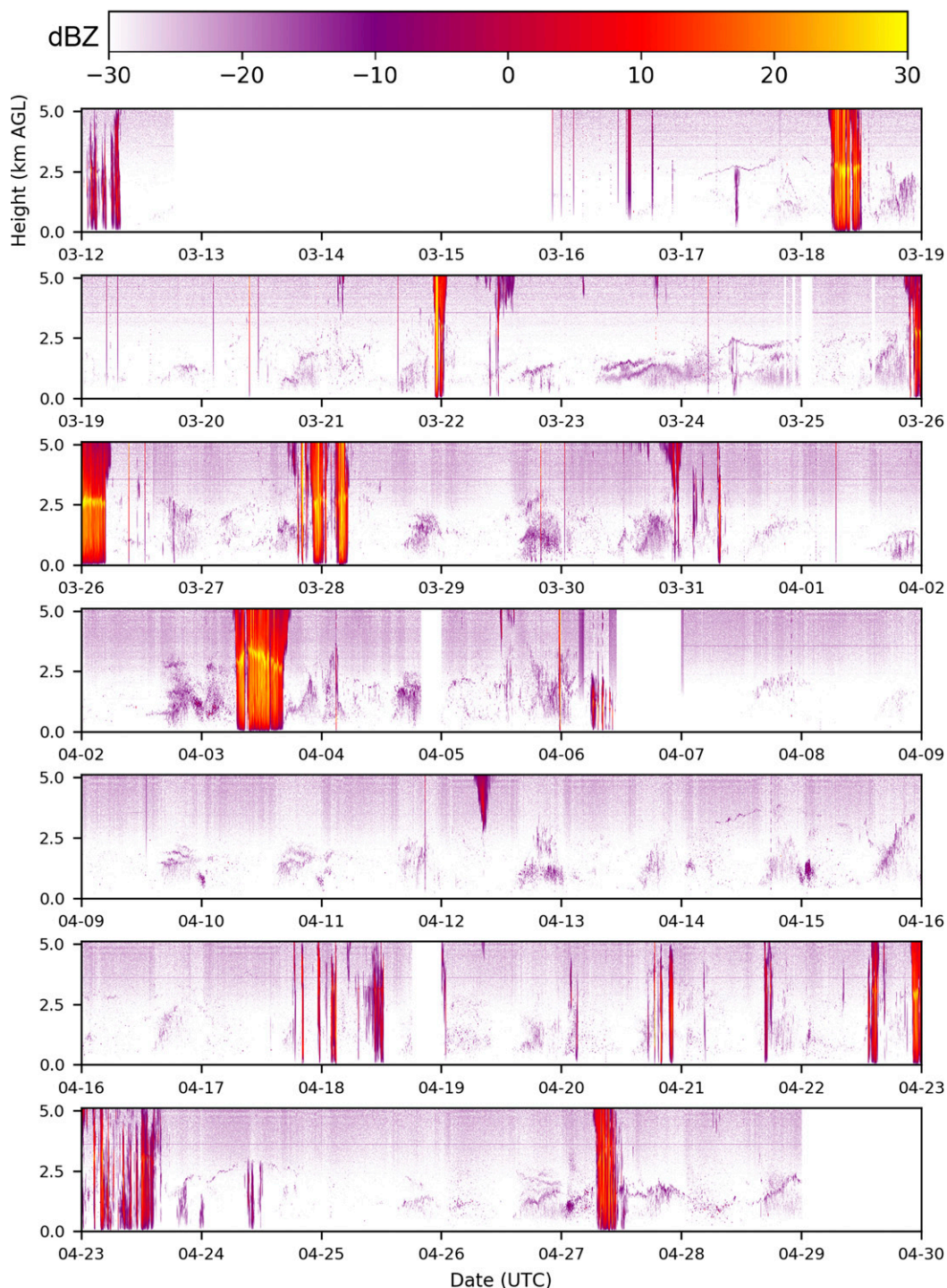


FIG. 5. As in Fig. 4, but for the 2017 campaign.

fades from -15 to -30 dBZ over the 50–700 m AGL layer (Figs. 4 and 7a). The scatterer identification algorithm (described later) was developed using only observations from 2017, collected after the TWT

amplifier was replaced and these two types of artifacts were no longer an issue.

Second, Doppler radial (vertical) velocity observations were dealiased using an image processing technique

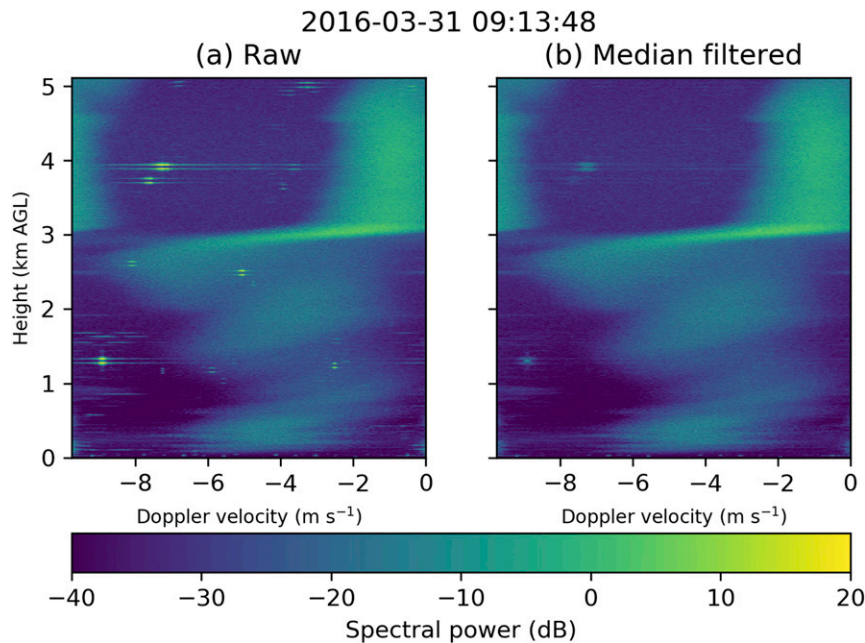


FIG. 6. UMass FMCW (a) raw and (b) median filtered spectral power (dB) as a function of Doppler velocity and height at 0914 UTC 31 May 2016 above Belle Mina. Application of a median filter to the raw spectra reduces the amplitude of most of the TWT power spur artifacts, but some stronger spurs (e.g., at 1.3 and 3.9 km AGL) persist. Some velocity aliasing can be seen at and above 3.0 km AGL (the top of the melting layer). Downward acceleration of precipitation can be seen within the melting layer (2.6 to 3.0 km AGL).

called *quality guided path unwrapping* (Herráez et al. 2002), for which a robust Python module exists (van der Walt et al. 2014). In testing, it was found that this algorithm, applied in two dimensions (time and height), performed well on UMass FMCW vertical velocity observations in moderate to heavy precipitation. Additionally, manual corrections to the dealiased Doppler velocity fields were necessary in the power spur-contaminated 2016 data (e.g., Fig. 7f), and in 2016 and 2017 data at times when radials were saturated by occasional echoes from unknown, highly reflective targets (likely low-flying aircraft at the Scottsboro airport; not shown).

Because the spatial variability (texture) of some variables can be used to distinguish some echo classes (Gourley et al. 2007; Lakshmanan et al. 2010; Penide et al. 2013), we also calculated the textures of the four main UMass FMCW variables. The texture T (spatial variability in the vertical) of a variable f at a height index h over a kernel size n is given by the root-mean-square-difference formula:

$$T(f_h) = \sqrt{\frac{\sum_{i=-(n-1)/2}^{(n-1)/2} (f_h - f_{h+i})^2}{n}}. \quad (1)$$

This texture formula is the same as that given by Gourley et al. [2007, their Eq. (1)] but reduced to a single (vertical) spatial dimension. A threshold of $T(\sigma_w) > 0.2 \text{ m s}^{-1}$ was found by inspection to be useful for demarcating contaminated precipitation observations (e.g., Fig. 8e). We did not dealias w at gates flagged by this method.

3. Scatterer classification and applications

a. Separation of precipitation and nonprecipitation observations using fuzzy logic

Radars operating at S band (i.e., around 3 GHz) straddle two principal scattering regimes depending on the atmospheric conditions above the instrument. Under “clear-air” (i.e., nonprecipitating, bioscatterer-free) conditions, most scattering is in the Bragg regime, which is governed by the equation

$$\eta \approx 0.38 C_n^2 \lambda^{-1/3}, \quad (2)$$

where η is reflectivity, λ is the radar wavelength, and C_n^2 is the structure parameter for the refractive index n (e.g., Gossard 1990).

When scattering is dominated by hydrometeors and bioscatterers (e.g., Contreras and Frasier 2008) in the

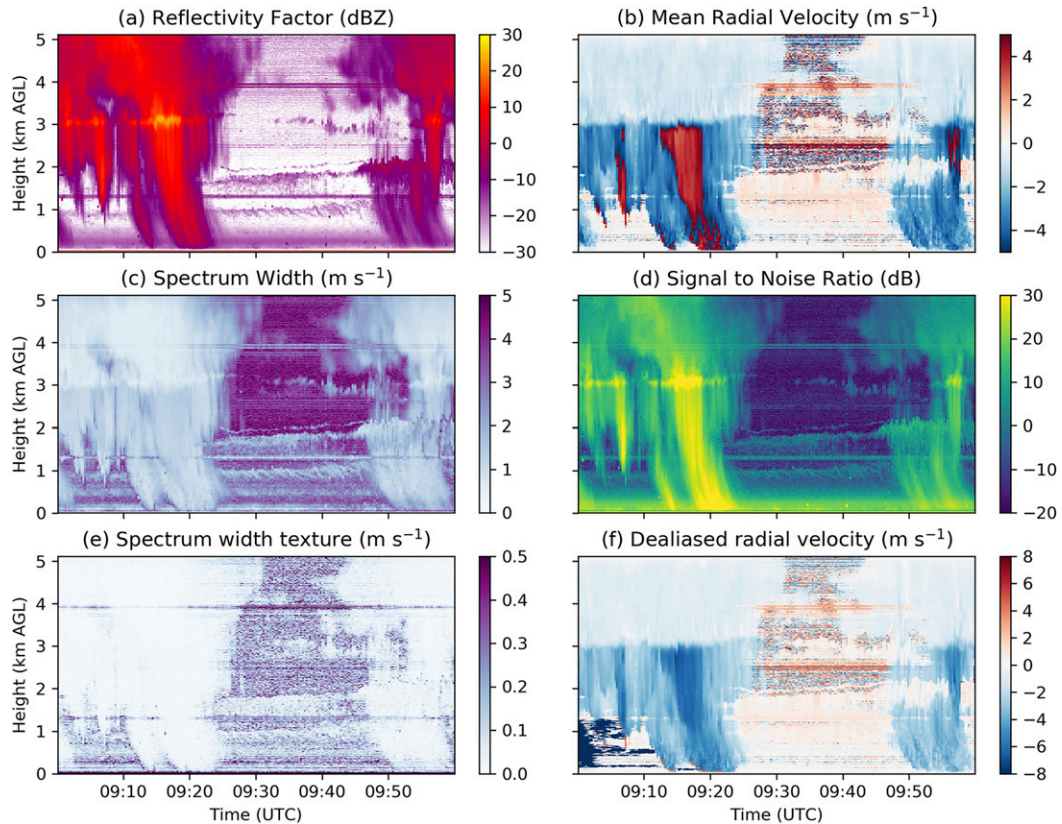


FIG. 7. As in Fig. 3, but for observations from 0900 to 1000 UTC 31 Mar 2016 over Belle Mina, showing an intermittent precipitation/virga event. The melting layer can be seen at 3.0 km AGL, and the top of the CBL is evident at about 2.0 km AGL, following the cessation of rain. These data were collected prior to the solid state amplifier upgrade and show the effects of power spurs (appearing as spurious echoes at constant height, e.g., at 1.3 and 3.9 km AGL) in all of the fields. These spurious echoes cause the automated dealiasing algorithm in (f) to fail from 0900 to 0920 UTC, below the precipitation.

Rayleigh regime ($D < \lambda/10$, where D is the particle diameter), reflectivity is governed by the equation

$$\eta \approx \frac{\pi^5}{\lambda^4} |K|^2 z, \quad (3)$$

where K is the complex dielectric constant of water, and z is the linear reflectivity factor of water spheres [e.g., Doviak and Zrnić 1993, their Eq. (4.31)]. Because the radar straddles these two very different scattering regimes, and because we wish to study the precipitation and nonprecipitation observations using different means, it is advantageous to automatically segregate regions dominated by precipitation and nonprecipitation by means of a scatterer classification algorithm. For example, it is necessary to isolate nonprecipitation observations in order to study the development of the convective BL in the absence of precipitation. As a second example, the UMass FMCW Doppler spectra collected near the surface can be compared to observations of drop size

distributions from a collocated Parsivel² disdrometer (Dawson et al. 2017), requiring isolation of gates containing precipitation.

Manual separation of precipitation and nonprecipitation observations in such a large dataset is subjective and time consuming. A number of studies have examined the problem of automatically discriminating precipitation and nonprecipitation echoes in observations from ground-based, single-polarized, S-band radars. In general, their focus has been on conically scanning radars, retaining precipitation observations while discarding nonprecipitation echoes such as those generated by anomalous propagation, ground clutter, bioscatterers, and nonmeteorological, nonbiological scatterers such as smoke and chaff (Fulton et al. 1998; Grecu and Krajewski 2000; Steiner and Smith 2002; Kessinger et al. 2003; Zhang et al. 2004; Lakshmanan et al. 2007, 2010). Because it points vertically, anomalous propagation and ground clutter are not significant issues for the UMass FMCW.

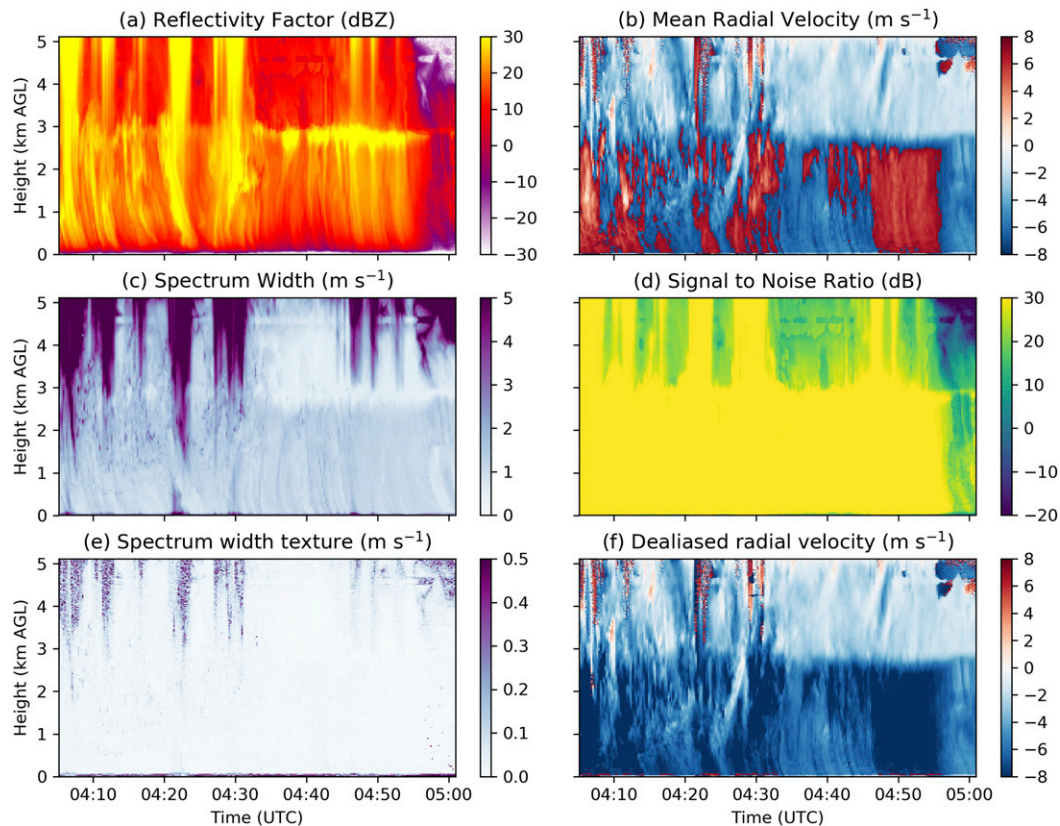


FIG. 8. As in Fig. 3, but for 0400–0500 UTC 28 Mar 2017, depicting a transition (at about 0430 UTC) from convective to stratiform precipitation around 0435 UTC. It can be seen that the heaviest convective precipitation is associated with relatively high spectrum width texture [in (e)] at and above 3 km AGL.

While bioscatterer echoes were often observed by the UMass FMCW, smoke and chaff releases were not documented during either the 2016 or 2017 deployments.

Using a simple Z threshold to separate Bragg and Rayleigh scatter-containing gates (e.g., Ralph 1995) proved problematic, as there was significant overlap between the two regimes at the S band within the CBL (spanning roughly from -35 to 10 dBZ). While heavy precipitation was relatively easy to distinguish using Z alone, regions of light precipitation, in-cloud precipitation, clouds, or strong Bragg scatter often fell into this ambiguous classification. Instead, we chose to use the generalized fuzzy logic technique described by Gourley et al. (2007). Fuzzy logic is a natural choice for this classification problem, as it has been extensively employed in scatterer classification schemes for polarimetric observations (Gourley et al. 2007; Park et al. 2009; Chandrasekar et al. 2013). Fuzzy logic was also used to discriminate nonprecipitation echoes in WSR-88D observations (Kessinger et al. 2003) before the nationwide WSR-88D dual-polarization upgrade of 2012–13.

Because UMass FMCW is a vertically pointing, single-polarized radar, polarimetric quantities used in WSR-88D hydrometeor classification algorithms (Park et al. 2009) were not available. The Gourley et al. (2007) technique, while developed for C-band polarimetric radar, is agnostic to the choice of band, polarimetry, and variables used in the classification. The only requirement is that sufficient differences exist in the measured variables between the classes to be assigned that their probability density functions (PDFs) have relatively small overlap. A user “trains” the algorithm using known examples of the desired classes. In this case, multihour subsets of UMass FMCW observations of known precipitation and nonprecipitation were isolated and used to generate the respective PDFs. The 9-h “precipitation” subset of the UMass FMCW data was composed of examples of stratiform, convective, and warm rain (i.e., no ice processes). The 9-h “nonprecipitation” subset contained observations of precipitation-free air, bioscatterer activity, or Bragg scatter in the CBL (Fig. 9). These two sets of training data were chosen to capture a plausible range of the

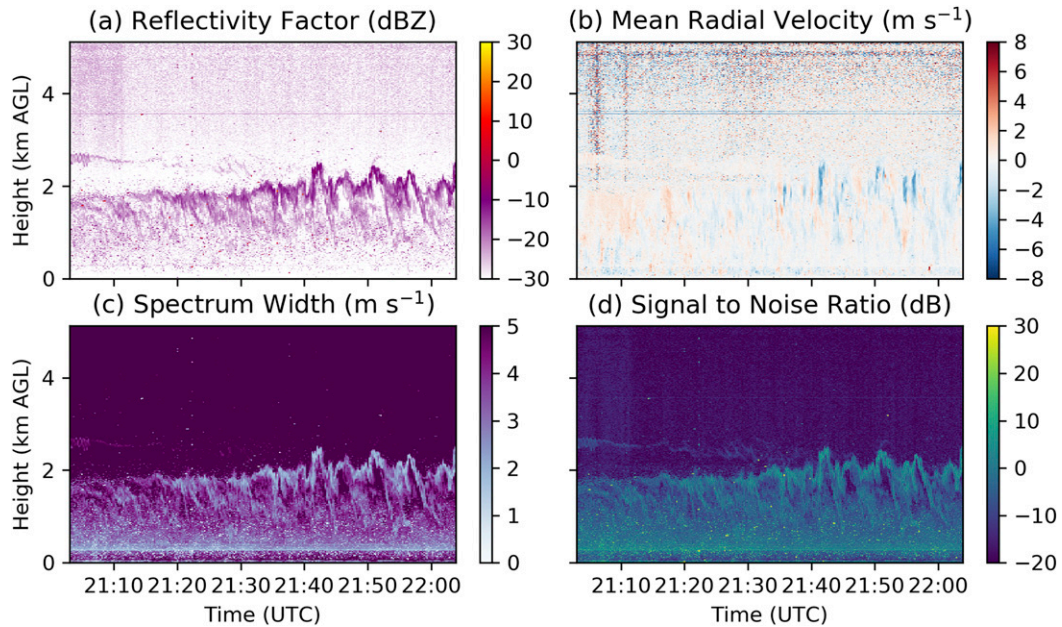


FIG. 9. As in Figs. 3a–d, but for 2100–2200 UTC 3 Apr 2017, showing the growth of the CBL.

measured and derived variables, and contained observations spanning the 2017 deployment period in order to account for any long-term variation in the radar’s performance. The fuzzy logic algorithm used in this study was trained on the four primary variables in the UMass FMCW data: Z , dealiased w (w_d), SNR, and σ_w , as well as their respective textures (Gourley et al. 2007). Because UMass FMCW is a vertically pointing radar, and has relatively low power sidelobes (with the first at -31 dB relative to the main lobe), ground clutter contamination (as in Gourley et al. 2007) is not a significant issue. Therefore, no ground clutter category was defined. One additional category, “no data,” was defined for those observations that were censored by the UMass FMCW signal processor for falling below the threshold of minimum detectable signal [-98.7 dBm (Table 1), which ranges from about -55 dBZ at 100 m AGL to -38 dBZ at 1 km AGL and -34 dBZ at 5 km AGL]. Such data are signified by a “flag” value of $Z = -99.0$ dBZ.

The Gaussian kernel density estimators (KDEs; Silverman 1986) were generated using the scikit-learn (Pedregosa et al. 2011) package for Python (Fig. 10). As in Gourley et al. (2007), the probability density functions (PDFs) were generated by summing together the individual Gaussian KDEs, then normalizing such that the area under each PDF was equal to unity. The overlap area of the PDFs was used to assign weights to each variable for each class. The smaller the PDF overlap area, the better a discriminator the variable was, and the larger the weight assigned to that variable.

The three variables found to have the largest weights were (in descending order) Z , SNR, and σ_w (Figs. 10a,c,d). Dealiasied radial velocity (w_d ; Fig. 10b) and all four texture fields (not shown) were found to have relatively small weights in comparison with the top three fields. The PDF for w_d for nonprecipitation exhibited artificially inflated “wings” close to the edges of the radar Nyquist interval (± 7.3 m s $^{-1}$; Fig. 10b). The wings were associated with low-SNR clear-air observations and could be eliminated by applying an SNR threshold. However, some low-SNR precipitation observations were also removed by this method (e.g., in contaminated precipitation observations near the top of the domain, or in fog and drizzle, not shown). Since this classification technique was intended to be applied to the entire dataset without any threshold values known a priori, we elected to retain these low-SNR observations of w_d in the training dataset. Therefore, despite previous studies that showed its potential power as a precipitation discriminator (Ralph et al. 1996), w_d was not included in the set of variables used to make the scatterer classifications in these data.

Once the gates were classified as predominantly precipitation or nonprecipitation using the PDFs for Z , SNR, and σ_w , the resulting fields were despeckled using a 3×3 median filter. This procedure eliminated erroneous classification of high-reflectivity point targets (likely bioscatterers) in the hydrometeor-free BL as precipitation. Since the median filter also removed most of the isolated no-data gates from the classification field,

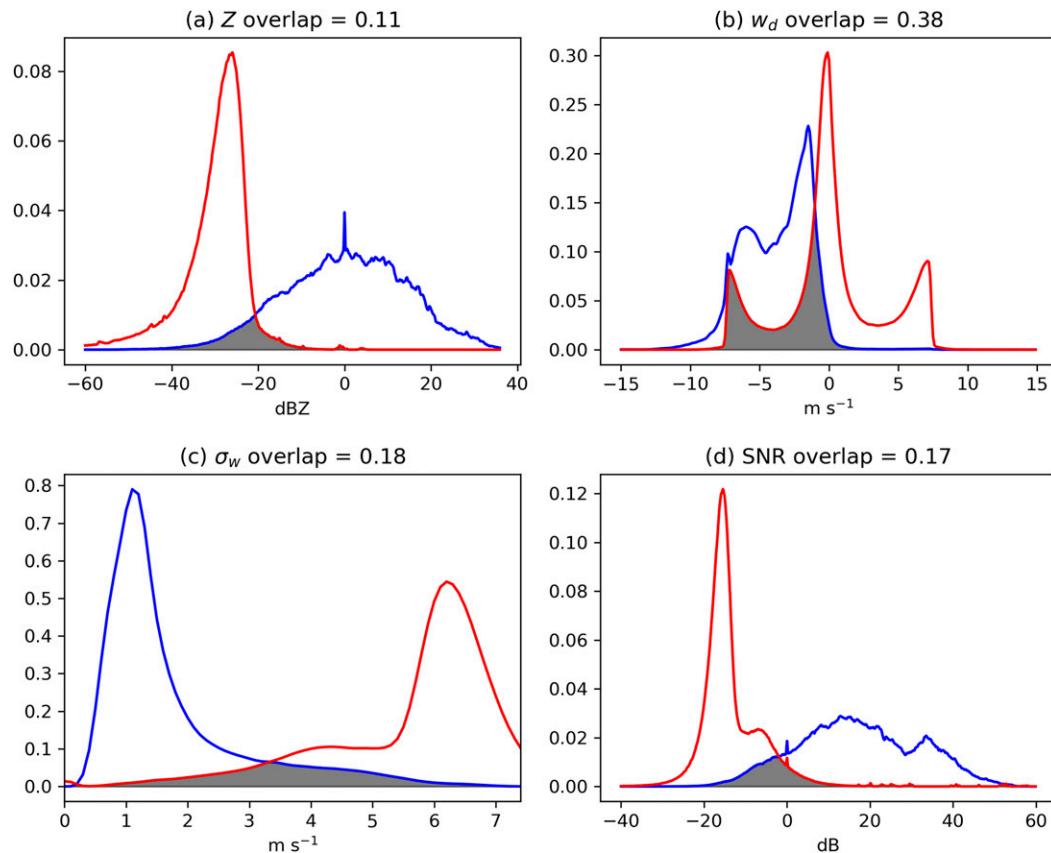


FIG. 10. Normalized probability density functions for (a) reflectivity (dBZ), (b) dealiased Doppler radial velocity ($m s^{-1}$), (c) spectrum width ($m s^{-1}$), and (d) SNR (dB) for precipitation (blue curves) and nonprecipitation (red curves). The normalized area where the two curves overlap (representing ambiguous classification) is shaded in dark gray.

the no-data gates were restored to the classification field following this procedure. Examples of the resulting classifications, generated from the UMass FMCW observations shown in Fig. 3 and Figs. 7–9, are shown in Fig. 11.

This classification scheme was applied to all of the 2016 and 2017 UMass FMCW observations (Figs. 12 and 13). We have applied the classification scheme based exclusively on 2017 UMass FMCW data naively to the 2016 data to assess the effects of the amplifier replacement (Waldinger et al. 2017). On first glance, the classification scheme algorithm appears to be working fairly well, with high-reflectivity regions and narrow zones at the top of the CBL (lightly precipitating cumulus) classed as precipitation. There are, however, a few issues of note. First, in the 2016 data (e.g., Figs. 11b and 12), the spurious echoes from the TWT power spurs are clearly misclassified as precipitation. Both the 2016 and 2017 observation periods were about seven weeks in length and collected during the same season (March–April), so we expect the percentages of gates classified

as precipitation and nonprecipitation to be comparable. However, 23.6% of all UMass FMCW observations from 2016 are classified as precipitation (Fig. 12), whereas only 7.6% of those from 2017 are (Fig. 13). If the gates known to be affected by power spurs and receiver saturation (section 2c) are eliminated from the 2016 calculation, the percentage of precipitation-classified gates decreases to 7.8%, a value nearly identical to that from 2017. This difference reinforces the notion that additional quality control needs to be performed on the UMass FMCW spectra collected in 2016 (e.g., Fig. 6)—work that is ongoing at the time of this writing.

Second, some regions near the top of the convective BL are classified as precipitation (e.g., Fig. 11a from 1640 UTC onward, Fig. 11d), but it is unclear whether the received echoes are from Bragg scatter, in-cloud precipitation, or a combination of the two. While vertical velocity oscillates from positive to negative in these regions (Fig. 9b), suggesting that Bragg scatter from refractive index turbulence at the tops of quasi-periodic

Scatterer classification

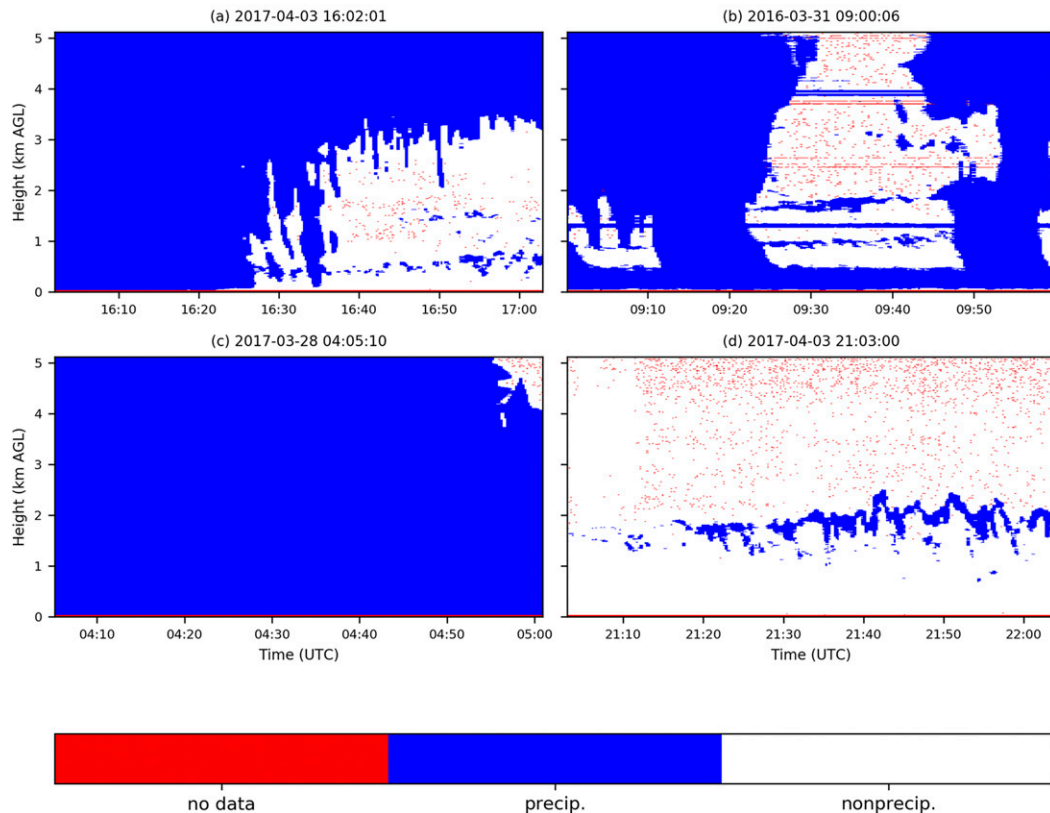


FIG. 11. Scatterer classification based upon the UMass FMCW observations shown in (a) Fig. 3, (b) Fig. 7, (c) Fig. 8, and (d) Fig. 9. White regions correspond to nonprecipitation observations, blue regions correspond to precipitation, and red pixels represent data points censored by the UMass FMCW signal processor.

thermal plumes is the dominant scattering mechanism, cloud bases (Fig. 14) were detected by a collocated Vaisala, Inc., CL31 ceilometer (Figs. 2b,c) in some instances (e.g., Fig. 14b), raising the possibility that in-cloud precipitation may also be present as has been observed in some tropical cumulus studies (e.g., Knight and Miller 1998). Additionally, the magnitude of the subsidence (-4 m s^{-1}) exceeds that of the ascent ($+2 \text{ m s}^{-1}$) (Fig. 9b), reinforcing the notion that gravity is pulling small precipitation particles earthward. We conclude that in such instances, when cloud bases (considered a precondition for precipitation) are not detected by the Vaisala cloud base detection algorithm (Ravala and Räsänen 2004), Bragg scatter is being misclassified as precipitation (e.g., Fig. 14a). However, when cloud bases and asymmetric subsiding motion are detected (e.g., Fig. 14b), we believe that in-cloud precipitation may be present but indistinguishable from Bragg scatter (mantle echoes) (e.g., Knight and Miller 1998). In the former case, the precipitation classification is incorrect, but in the

latter, it is partially correct. Unfortunately, corresponding WSR-88D polarimetric observations for the case depicted in Figs. 9b and 14b (not shown) do little to resolve the ambiguity owing to their relatively coarse vertical and temporal resolution. This result highlights the difficulty in differentiating S-band Bragg scatter from Rayleigh scatter in the CBL (Ralph et al. 1995; Knight and Miller 1998), even with high-resolution S-band radar observations.

b. Melting-layer (brightband) identification in precipitation

In preparation for converting Doppler spectra associated with precipitation into drop size distributions, for comparison with those from a collocated OTT Hydromet GmbH Parsivel² disdrometer, we further subdivide the precipitation regions into frozen and liquid hydrometeor classes. Within the UMass FMCW precipitation observations, a “bright band” of enhanced Z (Austin and Bemis 1950), indicating the

2016 Scatterer Classification

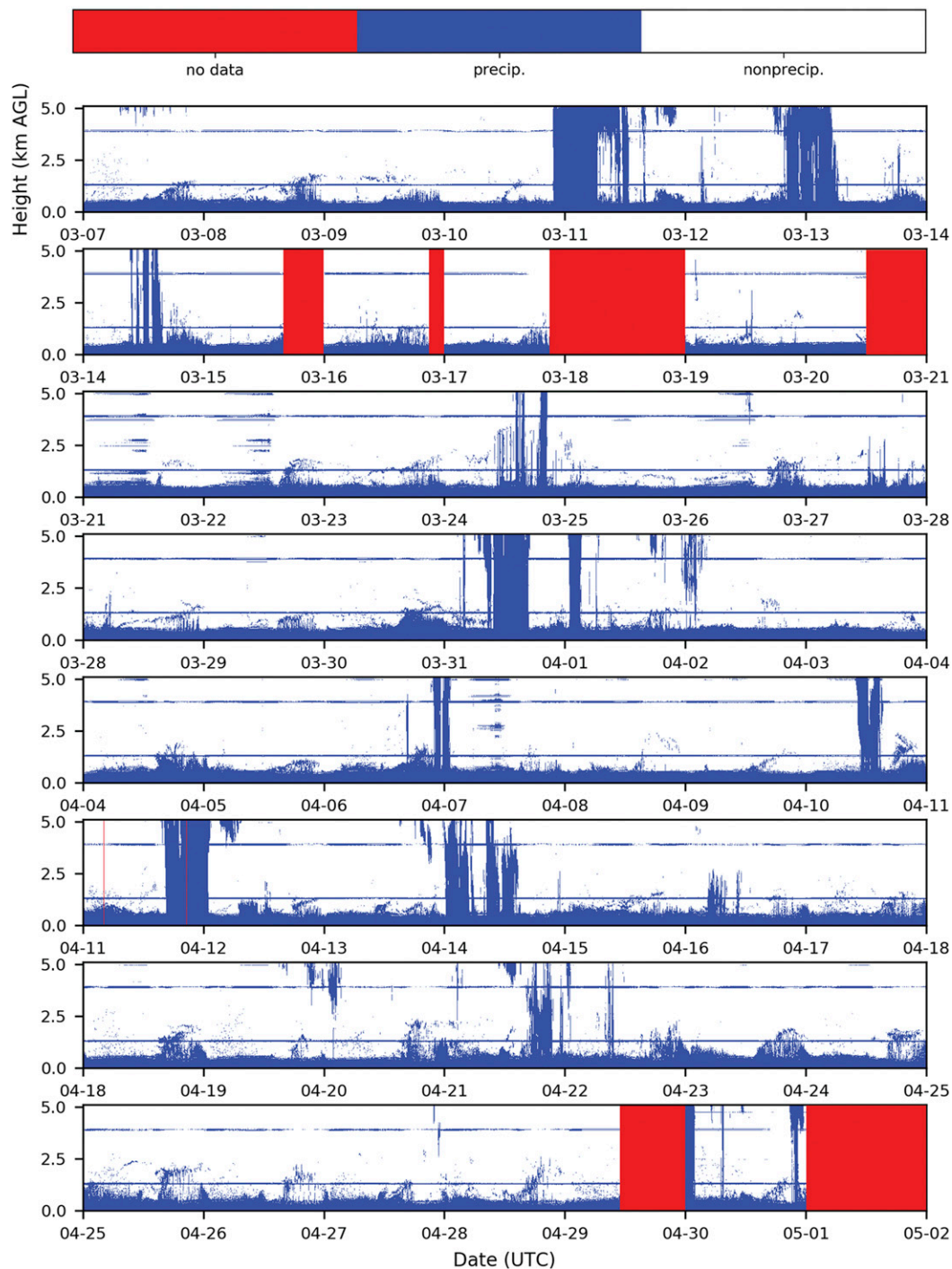


FIG. 12. Scatterer classifications based upon the 2016 UMass FMCW observations (Fig. 4).

presence of water-coated ice particles within the ML, was frequently observed in stratiform precipitation. In addition to serving as a natural separator of frozen and liquid hydrometeor classes, the bright band

strongly signifies nonconvective, stratiform precipitation rather than convective precipitation (Fabry and Zawadzki 1995; Rosenfeld et al. 1995; Biggerstaff and Listemaa 2000; Gourley and Calvert 2003; Qi et al. 2013).

2017 Scatterer Classification

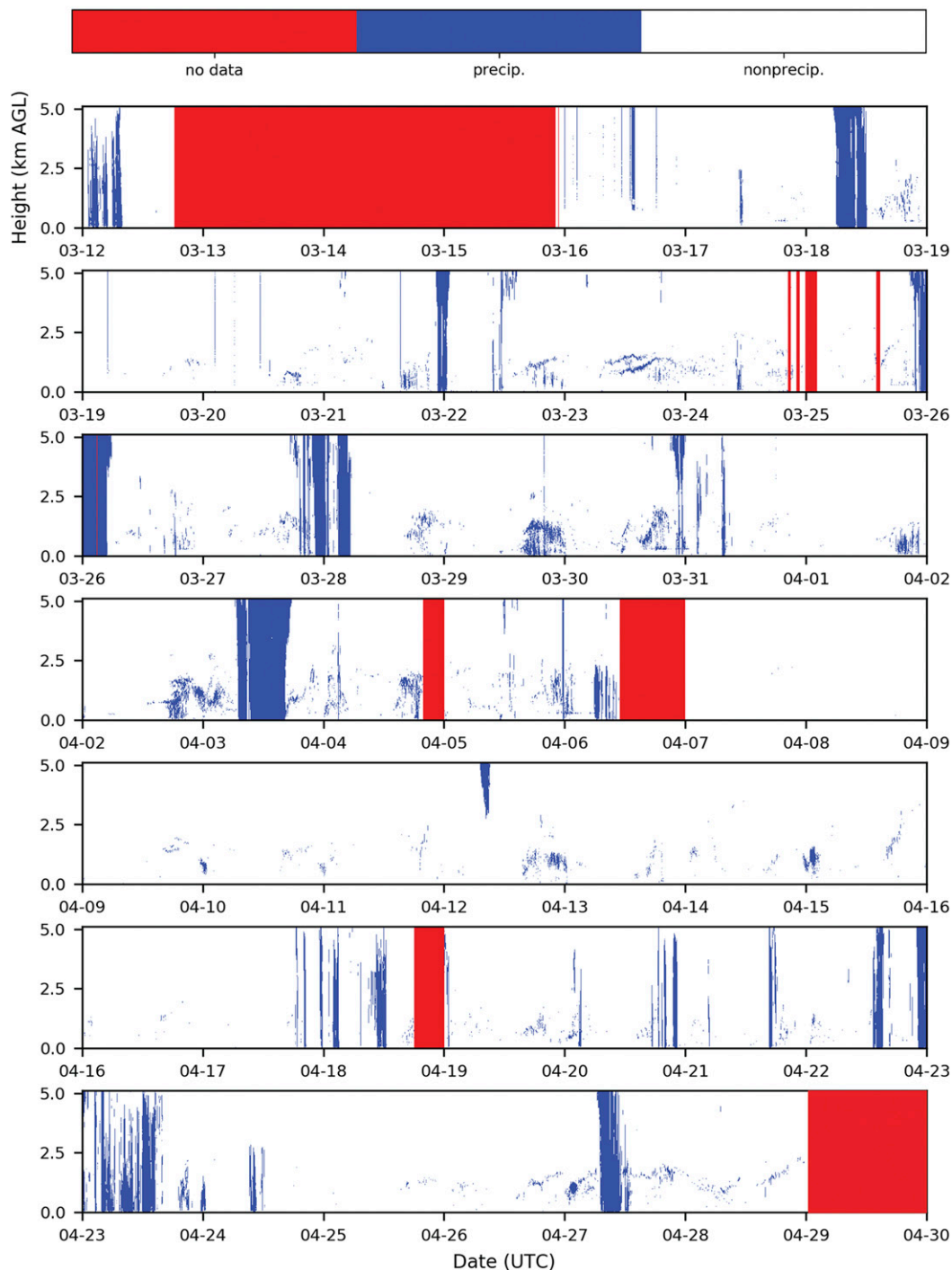


FIG. 13. As in Fig. 12, but based on the 2017 observations (Fig. 5).

Several methods have been proposed for automated detection of the ML using single-polarized radar observations; we focus on those employing derived vertical profiles of S-band reflectivity to determine a

single, representative ML identification for the column directly above the radar (Sánchez-Diezma et al. 2000; Zhang et al. 2008), as opposed to those utilizing information from a volume surrounding the radar to

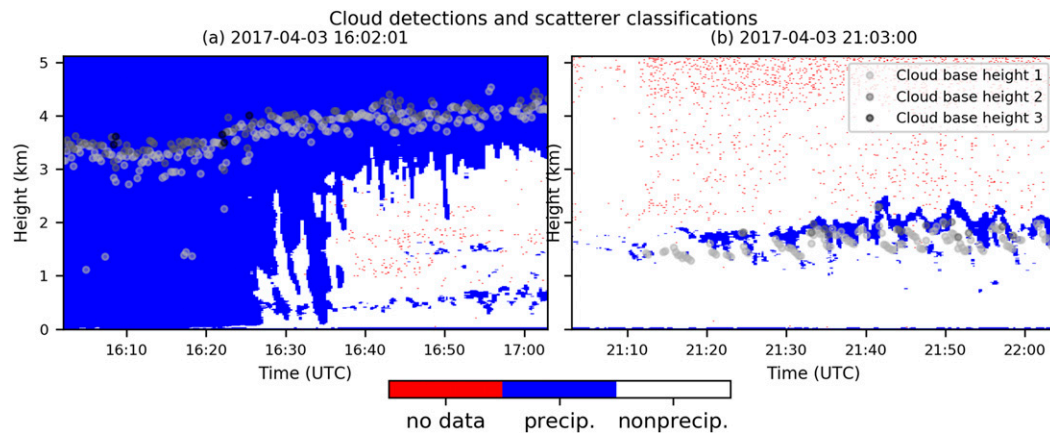


FIG. 14. Scatterer classification based upon the UMass FMCW observations shown in (a) Fig. 3 and (b) Fig. 9, overlaid with the first (light-gray dots), second (medium-gray dots), and third (black dots) cloud-base detections from a collocated Vaisala C31 ceilometer.

ascertain horizontal variability in ML height and thickness (Gourley and Calvert 2003).

Our method for BBID is patterned after that formulated by Zhang et al. (2008) for stratiform regions; the reader is referred to their paper for details. The principal differences in the present study are 1) we used measured vertical profiles of reflectivity from the UMass FMCW radar rather than vertical profiles of reflectivity derived from a volume coverage pattern, 2) we used estimated freezing-level height from an independent, collocated instrument rather than an operational numerical model fields as a first guess for the top of the ML, and 3) we used vertical velocity data from UMass FMCW to check the retrieved ML. The latter method is novel because the WSR-88D, for which the BBID technique of Zhang et al. (2008) was designed, typically does not collect vertical velocity data above the radar site. The downward acceleration of the melting particles can serve as a check of the UMass FMCW-derived BBID. For simplicity, we assumed only a single ML, excluding any double- or multiple-brightband structures (Ikeda et al. 2005; Martner et al. 2007; Emory et al. 2014).

The BBID was performed sequentially in time. Zhang et al.'s (2008) BBID algorithm requires a first guess for the altitude of the top of the ML. In their algorithm, the first guess is the 0°C height extracted from NOAA Rapid Refresh model temperature analyses. In our implementation, at each UMass FMCW observation time, the 0°C height was derived from the Atmospheric Emitted Radiance Interferometer (AERI; Knuteson et al. 2004a,b) optimal-estimation (AERIOe; Turner and Löhnert 2014) product of the Collaborative Lower Atmospheric Profiling System (Wagner et al. 2019). CLAMPS was collocated with UMass FMCW for both the 2016 and 2017 VORTEX-SE field campaigns

(Turner 2016, 2017; Lyza et al. 2018). The CLAMPS temperature profiles are derived from downwelling radiance measurements collected by the onboard AERI, and have root-mean-square errors of less than 1.0 K in clear-sky conditions up to 5 km AGL when compared with radiosonde temperature profiles (Turner and Löhnert 2014). One drawback to using CLAMPS temperature profiles for this purpose is that the hatch covering the AERI closes during precipitation to protect the instrument from water ingress. Therefore, CLAMPS T profiles are typically not available during precipitation, when BBID is performed. In these instances, we linearly interpolated the 0°C height from the “good” (blue dots in Fig. 15) CLAMPS T profiles to the first BBID time. The CLAMPS 0°C height sometimes exhibited substantial changes during lengthy precipitation events, which made it inadvisable to simply take the last retrieval prior to hatch closure. The height of the 0°C level over the Belle Mina site used in 2016 (altitude: 180 m MSL) ranged from 0 to 4.4 km AGL, with a median height of 3.3 km AGL. The 0°C level over the 2017 Scottsboro site (altitude: 198 m MSL) ranged from 0 to 4.9 km AGL, with a median height of 3.0 km AGL.

The algorithm proceeds as does that of Zhang et al. (2008) from this point on. The UMass FMCW precipitation classification (e.g., Figs. 11–13) was used to constrain the BBID to precipitation regions only. To reduce unsteadiness in the identified MLs with time, the brightband top and bottom time series are smoothed using a 5-min rolling average with a triangular window. The length of the window is comparable to the update period of the WSR-88D. Identified MLs are shown in Figs. 16 and 17 for two example rain events observed at the Scottsboro airport during the 2017 campaign. The first (Fig. 16) is a 10-h, mostly stratiform precipitation event on 3 April 2017 [prior to intensive operating

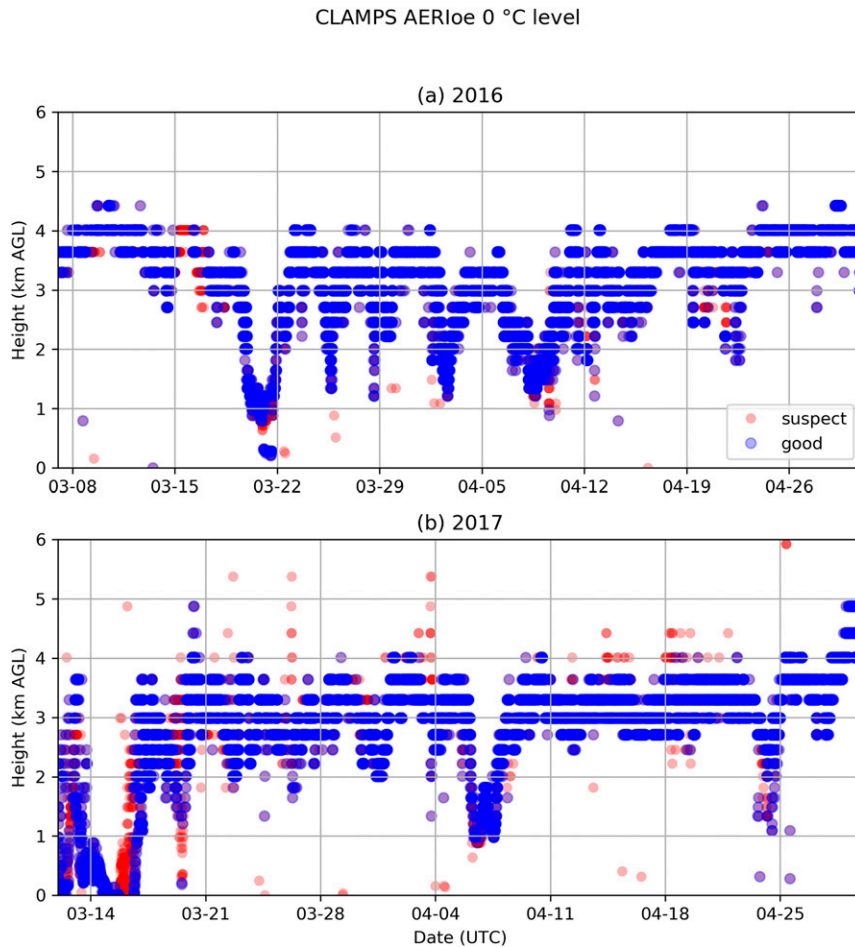


FIG. 15. Time series of the height of the 0°C level (km AGL) from CLAMPS AERIOe temperature profiles collected during VORTEX-SE in (a) 2016 (at Belle Mina) and (b) 2017 (at Scottsboro). Semitransparent blue or red dots indicate freezing-level heights from AERIOe retrievals flagged as good or suspect quality, respectively. Suspect heights were not used in this study.

period (IOP) 3A; Fig. 16d], and the second (Fig. 17) is a mixed convective–stratiform precipitation event on 27 April 2017 (prior to IOP 4A; Fig. 17d). The ML in the former event is relatively uniform in thickness and height (Fig. 16c) when compared with that derived from the latter event (Fig. 17c), despite its longer duration. The mean and standard deviations of the ML depth in the 3 April 2017 event are 125 and 78 m, respectively. The mean and standard deviations of the ML depth in the 27 April 2017 event are 90 and 89 m, respectively. These differences are likely the result of the more convective, unsteady character of the 27 April 2017 event relative to the 3 April 2017 event (Fabry and Zawadzki 1995). In heavy, convective precipitation on 27 April 2017, the BBID sometimes failed to identify an ML altogether (e.g., around 0830 and 0930 UTC in Fig. 17c).

To validate the identified ML, we compared the bottom of the ML as determined by the BBID with the

vertical gradient of dealiased Doppler velocity $\nabla_z w_d$. The latter quantity is expected to reach a maximum value in the bottom half of the ML, as the internal ice matrices of melting snow particles collapse and the now-liquid raindrops accelerate to terminal velocity (White et al. 2002). As with the brightband top and bottom, the time series of maximum $\nabla_z w_d$ was smoothed using a 5-min rolling average with a triangular window. The Pearson correlation coefficient between the heights of the brightband bottom and the brightband top were 0.94 and 0.91 for the 3 April 2017 and 27 April 2017 events, respectively (Figs. 18a,c), indicating that the two quantities fluctuate in concert, as expected, and that the BBID algorithm is working properly. The Pearson correlation coefficient between the heights of the brightband bottom and the height of maximum $\nabla_z w_d$ were 0.58 and 0.62 for the 3 April 2017 and 27 April 2017 events, respectively (Figs. 18b,d). These modest correlation coefficients imply a moderately

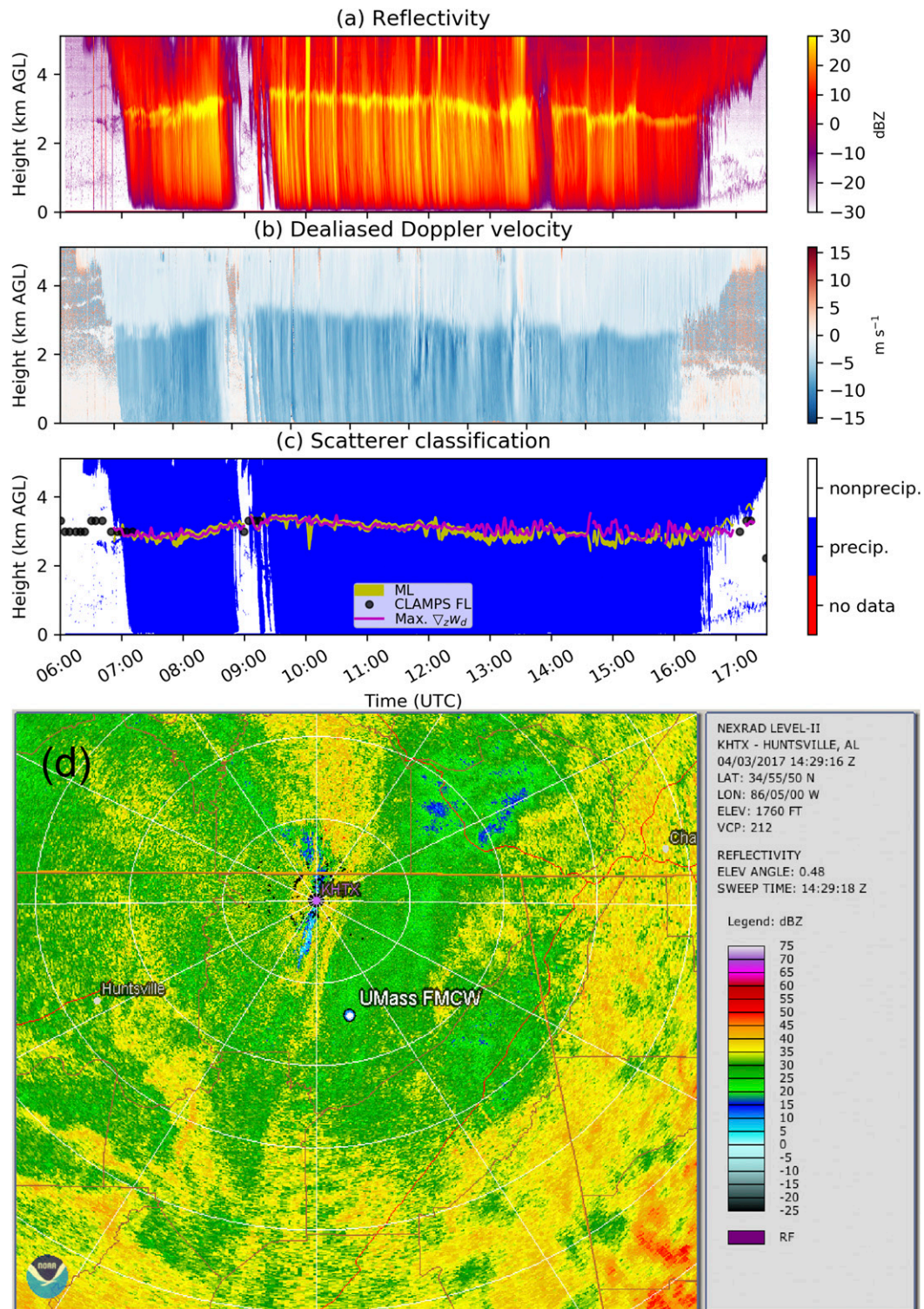
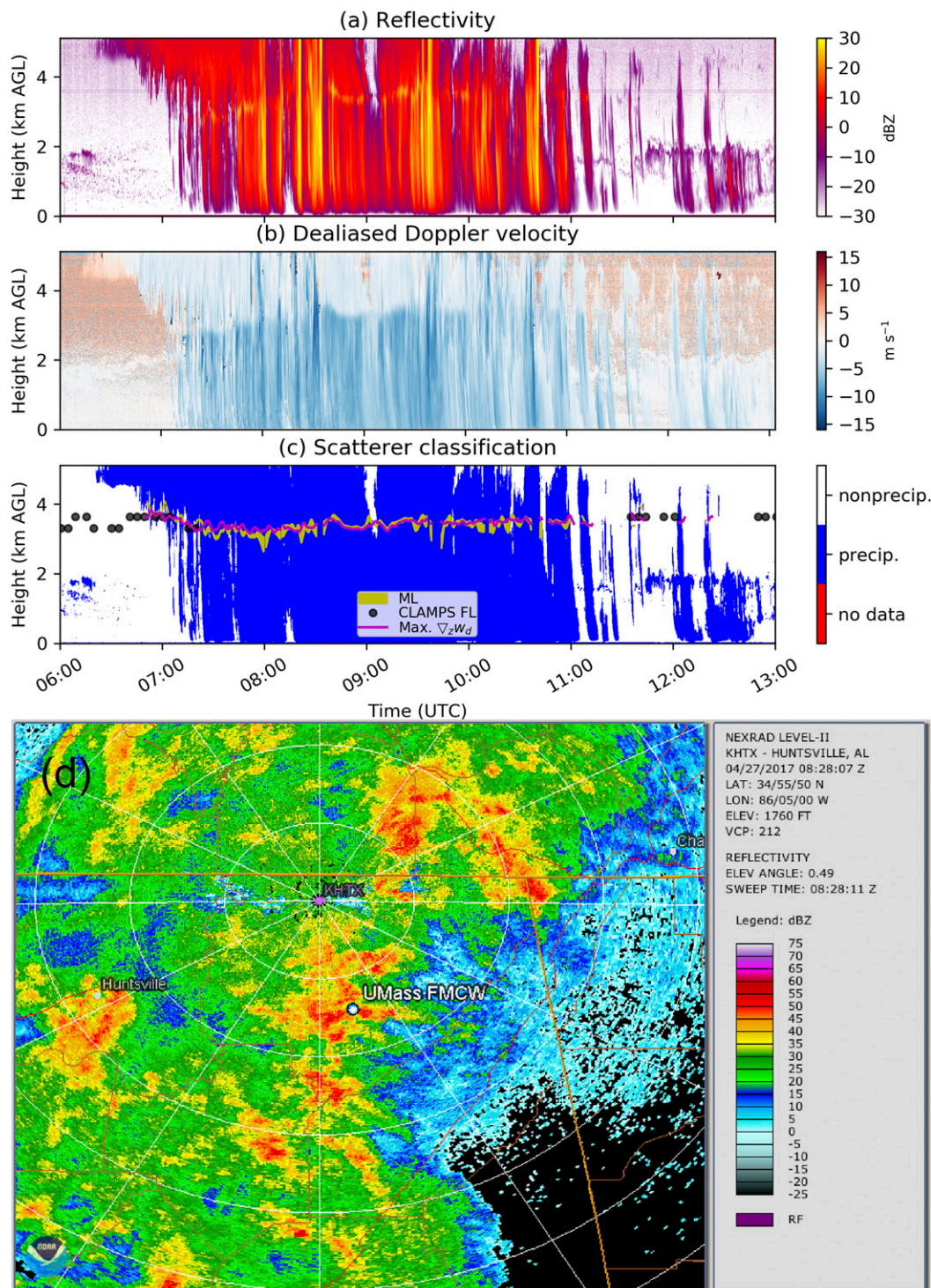


FIG. 16. (a) UMass FMCW reflectivity (dBZ) and (b) dealiased radial (vertical) velocity during a mostly stratiform precipitation event on 3 Apr 2017 (prior to IOP 3A). (c) Corresponding scatterer classification (as in Fig. 11), CLAMPS 0°C level (black dots), melting layer (yellow fill) identified using the BBID algorithm, and height of maximum vertical gradient in dealiased Doppler velocity (magenta line). (d) Reflectivity (dBZ) measured at an elevation angle of 0.5° by the WSR-88D at Hytop, Alabama (KHTX), at 1429 UTC 3 Apr 2017. Range rings and azimuth spokes are 20 km and 30° apart, respectively.



strong linear relationship between the height of the brightband bottom and the height of maximum downward acceleration of the precipitation particles. Other factors are likely increasing the dispersions of

these two quantities, including turbulence and microphysical processes such as collision, coalescence, aggregation, and breakup, which would modify the shapes of the Doppler spectra (Fabry and Zawadzki 1995).

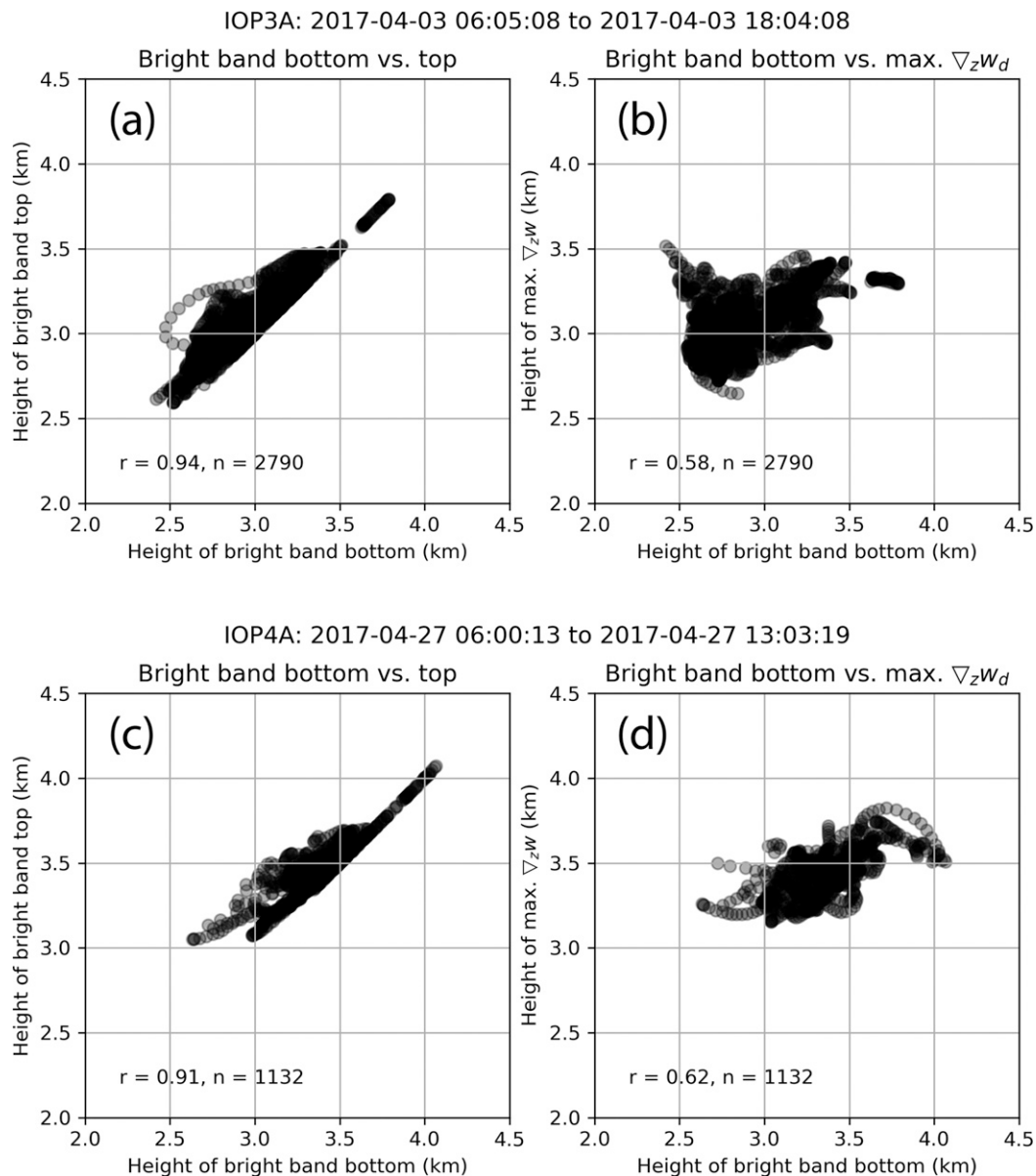


FIG. 18. Scatterplot of (left) brightband bottom height vs brightband top height and (right) brightband bottom height vs height of maximum vertical gradient of dealiased Doppler velocity for the precipitation events depicted in (a),(b) Fig. 16 and (c),(d) Fig. 17.

We consider the moderately strong relationship between these two variables further evidence that the BBID algorithm is working as expected, and that frozen, liquid, and mixed-phase hydrometers are being successfully separated.

c. CBL depth estimation using an extended Kalman filter-based technique

One of the stated objectives of VORTEX-SE was assessment of model representation of the BL structure and evolution prior to severe storms, via comparison

with high vertical and temporal resolution observations (Rasmussen 2015) such as those provided by UMass FMCW. In this context, we now turn our attention to the nonprecipitation observations identified using our scatterer classification algorithm, which make up the vast majority (>90%) of the observations by UMass FMCW during 2016 and 2017. (Figs. 12 and 13). Within this section, we assumed that Bragg scatter was the predominant mechanism generating echo in these regions, even though UMass FMCW can detect bioscatterers (Contreras and Frasier 2008) and some regions of Bragg

scatter may be misclassified as light precipitation (e.g., Fig. 14a).

A substantial number of studies, summarized by Seibert et al. (2000), detail the use of backscattered signal for CBL depth (or mixing height) detection. Lange et al. (2015) described a technique for automatic identification of the top of the CBL in UMass FMCW reflectivity observations using an extended Kalman filter (EKF)-based technique. This technique, which is based on former works of Rocadenbosch et al. (1998, 1999) in the lidar field, is predicated upon the assumption that in the vicinity of the mixed layer (ML)-to-free troposphere (FT) transition, the reflectivity decays as a complementary error function [$\text{erfc}(z) = 1 - \text{erf}(z)$] with height. At lidar frequencies, the entire ML provides strong returns (White et al. 1999; Cohn and Angevine 2000), so that the $\text{erfc}(z)$ model acceptably fits both the ML and ML-to-FT transition layers. At S-band frequencies, however, the reflectivity profile is expected to exhibit a local maximum at the top of the CBL (e.g., Fig. 5f of Ince et al. 2003). We therefore restrict our fitting of the erfc model to only the ML-to-FT transition layer in the UMass FMCW reflectivity profiles. In other words, the upper tail of the erfc function is matched to the reflectivity maximum, and the lower tail is matched to the FT reflectivity. Use of the EKF is beneficial because it maintains feature continuity over time and performs strong noise rejection. Performance of this technique has been evaluated against parameterizations in the Weather Research and Forecasting (WRF) numerical model under different synoptic conditions, and validated against lidar observations (Banks et al. 2015, 2016).

The filter operates by minimizing the error between the state vector parameterizing the model function and the true atmospheric one in a mean-square error sense over time. For a given time series of UMass FMCW reflectivity profiles, the EKF algorithm accepts a first guess for the CBL top height at the initial time (CBLH, as part of the state vector being initialized), and a small set of parameters describing, for example, the expected uncertainty of this initial guess and expected standard deviation of the CBLH around its mean value. The filter combines this information along with run-time estimates of the observation noise covariance matrix into its recursive loop. At each recursive step the filter iterates one step forward through the time series, fitting an $\text{erfc}(z)$ function to a smoothed version of the reflectivity profile (the median-filtered version of Fig. 6b) at each time. The EKF estimates the CBLH as the inflection point in the vertical derivative of the fitted reflectivity profile.

An example of this algorithm applied to a 2-h subset of the 2016 UMass FMCW reflectivity observations is

shown in Fig. 19a. On this date (31 March 2016), the CBL redeveloped in the wake of morning convective storms, and a tornadic storm formed east of Belle Mina later in the evening (LaFleur et al. 2018). It can be seen that the EKF-retrieved CBL depth underwent several fluctuations from 2200 31 March to 0000 UTC 1 April (Fig. 19a). For the 2016 data, the EKF algorithm was modified to avoid identifying the spurious echo artifact at 1.3 km AGL from the TWT power spur as being the top of the BL. It can be seen that algorithm successfully avoids misidentifying this artifact as the top of the BL at all but a handful of time steps, and then only at those time steps when the CBLH appears to coincide legitimately with the spur-contaminated height (Fig. 19a). The CBLH increased steadily from about 500 m at 2210 to 1.2 km at 2245 UTC, coincident with a period of sustained upward vertical motion (Fig. 19b) and cloud-free skies (Fig. 19c). Following the reappearance of clouds at 2240 UTC, the CBLH exceeded the cloud base height until 2300 UTC, indicating entrainment. Both the CBLH and cloud base height time series become highly variable, possibly owing to in-cloud turbulence (Grimsdell and Angevine 1998). Both covary moderately until 0000 UTC 1 April. It can be seen in the reflectivity (Fig. 19a) and vertical velocity (Fig. 19b) data that in-cloud precipitation is likely occurring in intermittent episodes over the radar site from 2300 to 0000 UTC, leading to enhanced vertical variability in both quantities. These processes are in accordance with the conceptual model presented in Fig. 1a (Stull 1988).

The thermodynamic CBL can be delineated in several different ways (Seidel et al. 2010). In general, the CBL is expected to exhibit well-mixed characteristics in both potential temperature and moisture (Stull 1988; Garratt 1992). We choose to inspect the vertical gradient of virtual potential temperature ($\nabla_z \theta_v$), which is expected to be near 0 K km^{-1} within the CBL and locally maximized at the top of the CBL (Stull 1988; Seidel et al. 2010). We generated profiles of $\nabla_z \theta_v$ from the coincident CLAMPS thermodynamic retrievals for the time series shown in Fig. 19a (Fig. 19d). The height of the local maximum in CLAMPS $\nabla_z \theta_v$ above the well mixed layer (stars in Fig. 19d) compares well to the CBL depth determined from the UMass FMCW reflectivity observations by the Lange et al. (2015) EKF technique (crosses in Fig. 19d), with a root-mean-square difference of 170 m. The estimates differ markedly, however, before 2220 UTC, with EKF-based CBL top heights too low, well below the cloud base height (Fig. 19c) and embedded within the well-mixed CBL (i.e., where $\nabla_z \theta_v \sim 0 \text{ K km}^{-1}$; Fig. 19d). This early period may correspond to the spinup time of the EKF,

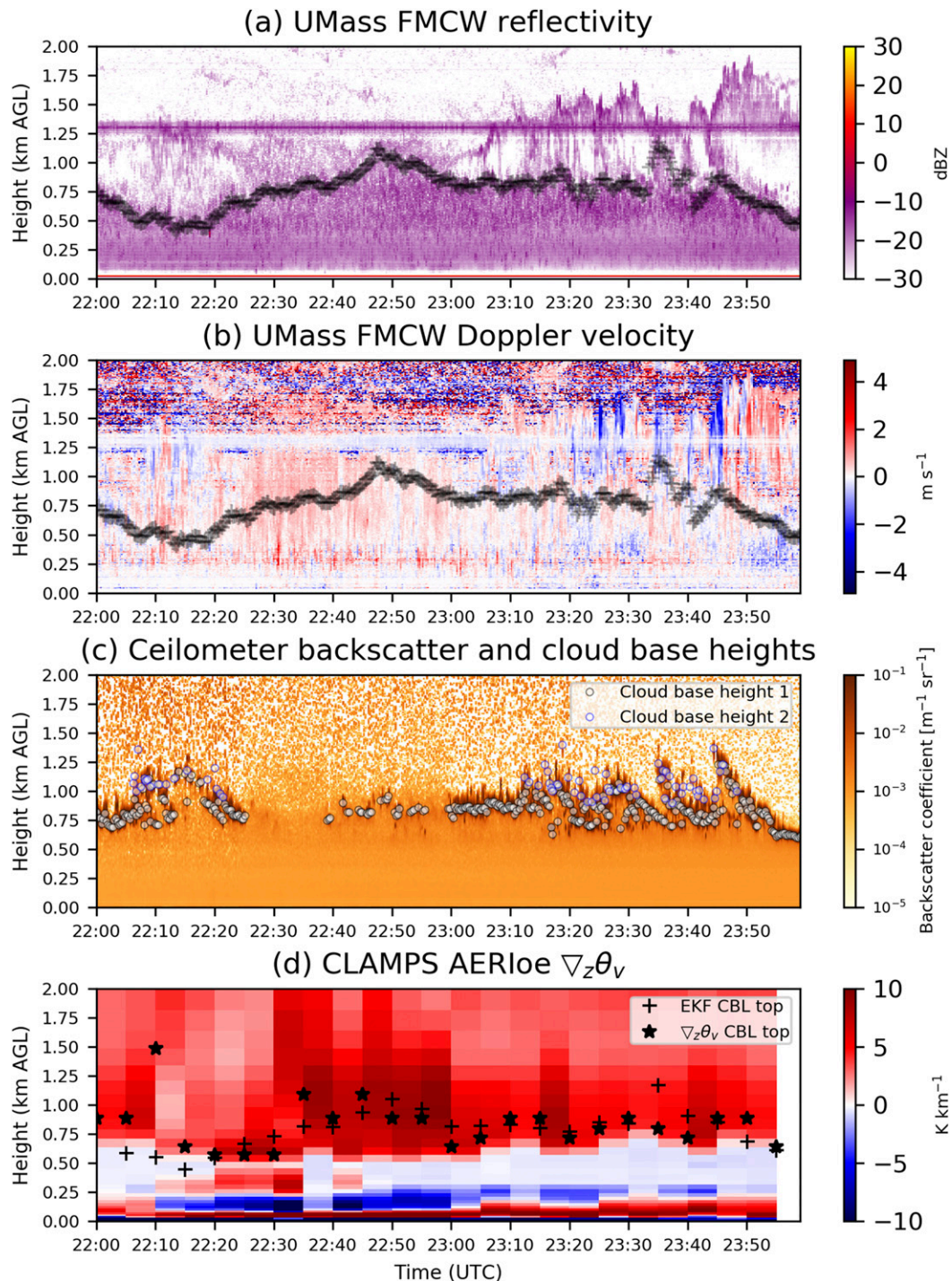


FIG. 19. (a) UMass FMCW reflectivity (dBZ) and (b) Doppler radial (vertical) velocity (m s^{-1}) from 2200 to 2300 UTC 31 Mar 2016 over Belle Mina. The plus signs denote CBL top heights as determined by the EKF-based algorithm of Lange et al. (2015). (c) Vaisala CL31 attenuated backscatter coefficient ($\text{m}^{-1} \text{sr}^{-1}$) and cloud-base height detections (black and blue open circles). (d) Vertical gradient of virtual potential temperature calculated from the CLAMPS profiles. The black plus signs denote the same heights shown by the plus signs in (a), interpolated to the CLAMPS profile times.

which was initialized at 2200 UTC. Excluding the period 2200–2220 UTC reduces the root-mean-square difference in CBLH calculated using the two methods to 130 m.

The CBLH tracking technique of Lange et al. (2015) holds promise for a more comprehensive, objective characterization of BL evolution over the VORTEX-SE domain. Application of this EKF-based algorithm to nonprecipitation observations spanning the entire 2016 and 2017 UMass FMCW VORTEX-SE datasets, as well as comparable datasets collected during other field campaigns, will be the subject of a future paper.

4. Conclusions

We developed a scatterer identification algorithm for observations collected during VORTEX-SE by a vertically pointing, S-band, single-polarized FMCW radar. This algorithm automatically separated UMass FMCW observations of precipitation and nonprecipitation and allowed for further identification of salient BL features of interest to the VORTEX-SE cohort. The products produced by our postprocessing include

- 1) dealiased vertical velocities in precipitation,
- 2) classification of UMass FMCW observations into precipitation, nonprecipitation, and no-data categories,
- 3) brightband top and bottom heights, allowing for separation of frozen, melting, and liquid hydrometeors in stratiform precipitation, and
- 4) convective boundary layer heights in nonprecipitation.

These products serve as a stepping stone toward a comprehensive characterization of the BL over northern Alabama during early spring. It may also be possible to add additional subclasses to the scatterer identification algorithm within the nonprecipitation class, specifically refractive index turbulence and biological scatterers (insects, birds, and bats), both of which were frequently sampled by UMass FMCW. At the time of this writing, these products are being used to derive conceptual models of CBL growth over the VORTEX-SE domain, and to estimate precipitation drop size distributions that can be verified by collocated disdrometer observations (Dawson et al. 2017) (Fig. 2c). Results from these two projects will be the subject of future papers.

Acknowledgments. This work was funded by NOAA Grants NA15OAR4590231 and NA16OAR4590208; Dr. Kevin Knupp of the University of Alabama Huntsville played critical facilitating roles in the deployment of the UMass FMCW in both 2016 and 2017. Drs. Temple Lee and Bruce Baker of NOAA secured

the use of land and electricity at the Belle Mina deployment site in 2016. The Python packages Matplotlib (Hunter 2007), scikit-image (van der Walt et al. 2014), scikit-learn (Pedregosa et al. 2011), cl2nc (<http://github.com/peterkuma/cl2nc> by Peter Kuma), and Py-ART (Helmus and Collis 2016) were used in the preparation of this paper, and Dr. Robert Jackson of Argonne National Laboratory provided the code for the texture calculations. CommSensLab is a María-de-Maeztu Unit of Excellence funded by the Agencia Estatal de Investigación (Spanish National Science Foundation). The sixth author's participation was supported via Spanish Government–European Regional Development Funds project TEC2015-63832-P. The authors gratefully acknowledge the substantive comments of three anonymous reviewers; the paper was markedly improved as a result of their interactions.

REFERENCES

- Angevine, W. M., A. B. White, and S. K. Avery, 1994: Boundary-layer depth and entrainment zone characterization with a boundary-layer profiler. *Bound.-Layer Meteor.*, **68**, 375–385, <https://doi.org/10.1007/BF00706797>.
- Atkins, N. T., M. L. Weisman, and L. J. Wicker, 1999: The influence of preexisting boundaries on supercell evolution. *Mon. Wea. Rev.*, **127**, 2910–2927, [https://doi.org/10.1175/1520-0493\(1999\)127<2910:TIOBPO>2.0.CO;2](https://doi.org/10.1175/1520-0493(1999)127<2910:TIOBPO>2.0.CO;2).
- Austin, P. M., and A. C. Bemis, 1950: A quantitative study of the “bright band” in radar precipitation echoes. *J. Meteor.*, **7**, 145–151, [https://doi.org/10.1175/1520-0469\(1950\)007<0145:AQSOTB>2.0.CO;2](https://doi.org/10.1175/1520-0469(1950)007<0145:AQSOTB>2.0.CO;2).
- Banghoff, J. R., D. J. Stensrud, and M. R. Kumjian, 2018: Convective boundary layer depth estimation from S-band dual-polarization radar. *J. Atmos. Oceanic Technol.*, **35**, 1723–1733, <https://doi.org/10.1175/JTECH-D-17-0210.1>.
- Banks, R. F., J. Tiana-Alsina, F. Rocadenbosch, and J. M. Baldasano, 2015: Performance evaluation of the boundary-layer height from lidar and the weather research and forecasting model at an urban coastal site in the north-east Iberian Peninsula. *Bound.-Layer Meteor.*, **157**, 265–292, <https://doi.org/10.1007/s10546-015-0056-2>.
- , —, J. M. Baldasano, F. Rocadenbosch, A. Papayannis, S. Solomos, and C. G. Tzanis, 2016: Sensitivity of boundary-layer variables to PBL schemes in the WRF model based on surface meteorological observations, lidar, and radiosondes during the HygrA-CD campaign. *Atmos. Res.*, **176–177**, 185–201, <https://doi.org/10.1016/j.atmosres.2016.02.024>.
- Biggerstaff, M. I., and S. A. Listmaa, 2000: An improved scheme for convective/stratiform echo classification using radar reflectivity. *J. Appl. Meteor.*, **39**, 2129–2150, [https://doi.org/10.1175/1520-0450\(2001\)040<2129:AISFCS>2.0.CO;2](https://doi.org/10.1175/1520-0450(2001)040<2129:AISFCS>2.0.CO;2).
- Brown, R. A., V. T. Wood, R. M. Steadham, R. R. Lee, B. A. Flickinger, and D. Sirmans, 2005: New WSR-88D volume coverage pattern 12: Results of field tests. *Wea. Forecasting*, **20**, 385–393, <https://doi.org/10.1175/WAF848.1>.
- Chandrasekar, V., R. Keränen, S. Lim, and D. Moiseev, 2013: Recent advances in classification of observations from dual polarization weather radars. *Atmos. Res.*, **119**, 97–111, <https://doi.org/10.1016/j.atmosres.2011.08.014>.

- Cohn, S. A., and W. M. Angevine, 2000: Boundary layer height and entrainment zone thickness measured by lidars and wind-profiling radars. *J. Appl. Meteor.*, **39**, 1233–1247, [https://doi.org/10.1175/1520-0450\(2000\)039<1233:BLHAEZ>2.0.CO;2](https://doi.org/10.1175/1520-0450(2000)039<1233:BLHAEZ>2.0.CO;2).
- Contreras, R. F., and S. J. Frasier, 2008: High-resolution observations of insects in the atmospheric boundary layer. *J. Atmos. Oceanic Technol.*, **25**, 2176–2187, <https://doi.org/10.1175/2008JTECHA1059.1>.
- Crum, T. D., and R. L. Alberty, 1993: The WSR-88D and the WSR-88D operational support facility. *Bull. Amer. Meteor. Soc.*, **74**, 1669–1687, [https://doi.org/10.1175/1520-0477\(1993\)074<1669:TWATWO>2.0.CO;2](https://doi.org/10.1175/1520-0477(1993)074<1669:TWATWO>2.0.CO;2).
- Dawson, D. T., and Coauthors, 2017: Overview of Purdue's mobile disdrometer operations during VORTEX-SE 2016–2017. *38th Conf. on Radar Meteorology*, Chicago, Illinois, Amer. Meteor. Soc., 23A.2A, <https://ams.confex.com/ams/38RADAR/meetingapp.cgi/Paper/321195>.
- Demoz, B., and Coauthors, 2006: The dryline on 22 May 2002 during IHOP_2002: Convective-scale measurements at the profiling site. *Mon. Wea. Rev.*, **134**, 294–310, <https://doi.org/10.1175/MWR3054.1>.
- Doviak, R. J., and D. S. Zrnić, 1993: *Doppler Weather Radar and Observations*. 2nd ed. Academic Press, 562 pp.
- Eaton, F. D., S. A. McLaughlin, and J. R. Hines, 1995: A new frequency-modulated continuous wave radar for studying planetary boundary layer morphology. *Radio Sci.*, **30**, 75–88, <https://doi.org/10.1029/94RS01937>.
- Emory, A. E., B. Demoz, K. Vermeesch, and M. Hicks, 2014: Double bright band observations with high-resolution vertically pointing radar, lidar, and profilers. *J. Geophys. Res. Atmos.*, **119**, 8201–8211, <https://doi.org/10.1002/2013JD020063>.
- Fabry, F., and I. Zawadzki, 1995: Long-term radar observations of the melting layer of precipitation and their interpretation. *J. Atmos. Sci.*, **52**, 838–851, [https://doi.org/10.1175/1520-0469\(1995\)052<0838:LTROOT>2.0.CO;2](https://doi.org/10.1175/1520-0469(1995)052<0838:LTROOT>2.0.CO;2).
- , G. L. Austin, and D. Tees, 1992: The accuracy of rainfall estimates by radar as a function of range. *Quart. J. Roy. Meteor. Soc.*, **118**, 435–453, <https://doi.org/10.1002/qj.49711850503>.
- Frasier, S. J., and J. Waldinger, 2016: UMass S-band FMCW Profiling Radar data, in netCDF format. Version 1.0, UCAR/NCAR Earth Observing Laboratory, accessed 8 June 2016, <https://doi.org/10.5065/D67P8WS3>.
- , T. Ince, and F. J. Lopez-Dekker, 2002: Performance of S-band FMCW radar for boundary layer observation. *15th Conf. on Boundary Layer and Turbulence*, Wageningen, Netherlands, Amer. Meteor. Soc., 7.7, <https://ams.confex.com/ams/BLT/webprogram/Paper44067.html>.
- , J. Waldinger, W. Heberling, R. L. Tanamachi, and D. T. Dawson II, 2017: UMass FMCW Radar Data. Version 1.0, UCAR/NCAR Earth Observing Laboratory, accessed 8 June 2016, <https://doi.org/10.5065/D6N0158V>.
- Fulton, R. A., J. P. Breidenbach, D.-J. Seo, D. A. Miller, and T. O'Bannon, 1998: The WSR-88D rainfall algorithm. *Weather Forecasting*, **13**, 377–395, [https://doi.org/10.1175/1520-0434\(1998\)013<0377:TWRA>2.0.CO;2](https://doi.org/10.1175/1520-0434(1998)013<0377:TWRA>2.0.CO;2).
- Garratt, J. R., 1992: *The Atmospheric Boundary Layer*. Cambridge University Press, 316 pp.
- Giangrande, S. E., T. Toto, A. Bansemmer, M. R. Kumjian, S. Mishra, and A. V. Ryzhkov, 2016: Insights into riming and aggregation processes as revealed by aircraft, radar, and disdrometer observations for a 27 April 2011 widespread precipitation event. *J. Geophys. Res. Atmos.*, **121**, 5846–5863, <https://doi.org/10.1002/2015JD024537>.
- Gossard, E. E., 1990: Radar Research on the Atmospheric Boundary Layer. *Radar in Meteorology: Battan Memorial and 40th Anniversary Radar Meteorology Conference*, D. Atlas, Ed., Amer. Meteor. Soc., 477–527.
- , and R. G. Strauch, 1983: *Radar Observations of Clear Air and Clouds*. Developments in Atmospheric Sciences, Vol. 110, John Wiley and Sons, 280 pp.
- Gourley, J. J., and C. M. Calvert, 2003: Automated detection of the bright band using WSR-88D data. *Wea. Forecasting*, **18**, 585–599, [https://doi.org/10.1175/1520-0434\(2003\)018<0585:ADOTBB>2.0.CO;2](https://doi.org/10.1175/1520-0434(2003)018<0585:ADOTBB>2.0.CO;2).
- , P. Tabary, and J. Parent du Chatelet, 2007: A fuzzy logic algorithm for the separation of precipitating from non-precipitating echoes using polarimetric radar observations. *J. Atmos. Oceanic Technol.*, **24**, 1439–1451, <https://doi.org/10.1175/JTECH2035.1>.
- Greco, M., and W. F. Krajewski, 2000: An efficient methodology for detection of anomalous propagation echoes in radar reflectivity data using neural networks. *J. Atmos. Oceanic Technol.*, **17**, 121–129, [https://doi.org/10.1175/1520-0426\(2000\)017<0121:AEMFDO>2.0.CO;2](https://doi.org/10.1175/1520-0426(2000)017<0121:AEMFDO>2.0.CO;2).
- Grimsdell, A. W., and W. M. Angevine, 1998: Convective boundary layer height measurement with wind profilers and comparison to cloud base. *J. Atmos. Oceanic Technol.*, **15**, 1331–1338, [https://doi.org/10.1175/1520-0426\(1998\)015<1331:CBLHMW>2.0.CO;2](https://doi.org/10.1175/1520-0426(1998)015<1331:CBLHMW>2.0.CO;2).
- Heinselman, P. L., P. L. Spencer, K. L. Elmore, D. J. Stensrud, R. M. Hluchan, and P. C. Burke, 2009: Radar reflectivity-based estimates of mixed layer depth. *J. Atmos. Oceanic Technol.*, **26**, 229–239, <https://doi.org/10.1175/2008JTECHA1091.1>.
- Helmus, J. J., and S. Collis, 2016: The Python ARM Radar Toolkit (Py-ART), a library for working with weather radar data in the Python programming language. *J. Open Res. Software*, **4**, e25, <https://doi.org/10.5334/jors.119>.
- Herráez, M. A., D. R. Burton, M. J. Lalor, and M. A. Gdeisat, 2002: Fast two-dimensional phase-unwrapping algorithm based on sorting by reliability following a noncontinuous path. *Appl. Opt.*, **41**, 7437–7444, <https://doi.org/10.1364/AO.41.007437>.
- Hunter, J. D., 2007: Matplotlib: A 2D graphics environment. *Comput. Sci. Eng.*, **9**, 90–95, <https://doi.org/10.1109/MCSE.2007.55>.
- Ikeda, K., E. A. Brandes, and R. M. Rasmussen, 2005: Polarimetric radar observation of multiple freezing levels. *J. Atmos. Sci.*, **62**, 3624–3636, <https://doi.org/10.1175/JAS3556.1>.
- Ince, T., A. L. Pazmany, and S. J. Frasier, 2000: High resolution profiling of the atmospheric boundary layer. *IGARSS 2000: IEEE 2000 Int. Geoscience and Remote Sensing Symp.*, Honolulu, HI, IEEE, 209–211, <https://doi.org/10.1109/IGARSS.2000.860470>.
- , S. J. Frasier, A. Muschinski, and A. L. Pazmany, 2003: An S-band frequency-modulated continuous-wave boundary layer profiler: Description and initial results. *Radio Sci.*, **38**, 1072, <https://doi.org/10.1029/2002RS002753>.
- Kessinger, C. J., S. Ellis, and J. V. Andel, 2003: The radar echo classifier: A fuzzy logic algorithm for the WSR-88D. *Third Conf. on Artificial Intelligence Applications to the Environmental Science*, Long Beach, California, Amer. Meteor. Soc., P1.2, <https://ams.confex.com/ams/annual2003/webprogram/Paper54946.html>.
- Knight, C. A., and L. J. Miller, 1998: Early radar echoes from small, warm cumulus: Bragg and hydrometeor scattering. *J. Atmos. Sci.*, **55**, 2974–2992, [https://doi.org/10.1175/1520-0469\(1998\)055<2974:EREFWS>2.0.CO;2](https://doi.org/10.1175/1520-0469(1998)055<2974:EREFWS>2.0.CO;2).
- Knuteson, R. O., and Coauthors, 2004a: Atmospheric emitted radiance interferometer. Part II: Instrument performance.

- J. Atmos. Oceanic Technol.*, **21**, 1777–1789, <https://doi.org/10.1175/JTECH-1663.1>.
- , and Coauthors, 2004b: Atmospheric emitted radiance interferometer. Part I: Instrument design. *J. Atmos. Oceanic Technol.*, **21**, 1763–1776, <https://doi.org/10.1175/JTECH-1662.1>.
- Koch, S., 2016: VORTEX-SE: Program and activities. *28th Conf. on Severe Local Storms*, Portland, Oregon, Amer. Meteor. Soc., 3.1, <https://ams.confex.com/ams/28SLS/webprogram/Paper300782.html>.
- LaFleur, A. T., R. L. Tanamachi, D. T. Dawson II, S. J. Frasier, J. Waldinger, and D. D. Turner, 2018: The role of direct insolation and near-surface moisture advection in the recovery of CAPE on 31 March 2016 during VORTEX-Southeast. *29th Conf. on Severe Local Storms*, Stowe, Vermont, Amer. Meteor. Soc., 292, <https://ams.confex.com/ams/38RADAR/webprogram/Paper320614.html>.
- Lakshmanan, V., A. Fritz, T. Smith, K. Hondl, and G. Stumpf, 2007: An automated technique to quality control radar reflectivity data. *J. Climate Appl. Meteor.*, **46**, 288–305, <https://doi.org/10.1175/JAM2460.1>.
- , J. Zhang, and K. Howard, 2010: A technique to censor biological echoes in radar reflectivity data. *J. Climate Appl. Meteor.*, **49**, 453–462, <https://doi.org/10.1175/2009JAMC2255.1>.
- Lange, D., F. Rocadenbosch, J. Tiana-Alsina, and S. J. Frasier, 2015: Atmospheric boundary layer height estimation using a Kalman filter and a frequency-modulated continuous-wave radar. *IEEE Trans. Geosci. Remote Sens.*, **53**, 3338–3349, <https://doi.org/10.1109/TGRS.2014.2374233>.
- Lee, T. R., M. Buban, E. Dumas, and C. B. Baker, 2018: On the use of rotary-wing aircraft to sample near-surface thermodynamic fields: Results from recent field campaigns. *Sensors*, **19**, <https://doi.org/10.3390/s19010010>.
- , —, D. D. Turner, T. P. Meyers, and C. B. Baker, 2019: Evaluation of the High-Resolution Rapid Refresh (HRRR) model using near-surface meteorological and flux observations from northern Alabama. *Wea. Forecasting*, **34**, 635–663, <https://doi.org/10.1175/WAF-D-18-0184.1>.
- Lyza, A. W., and K. R. Knupp, 2018: A background investigation of tornado activity across the Southern Cumberland Plateau terrain system of northeastern Alabama. *Mon. Wea. Rev.*, **146**, 4261–4278, <https://doi.org/10.1175/MWR-D-18-0300.1>.
- , —, D. D. Turner, R. A. Wade, and T. A. Murphy, 2018: Analyzing the effects of complex terrain in northeastern Alabama severe weather events using multiple profiling systems, Doppler Radar, and in situ measurements during the VORTEX-SE 2017 field campaign. *19th Symp. on Meteorological Observation and Instrumentation*, Austin, Texas, Amer. Meteor. Soc., 11.15, <https://ams.confex.com/ams/98Annual/webprogram/Paper336209.html>.
- Markowski, P. M., and Y. P. Richardson, 2009: Tornadogenesis: Our current understanding, forecasting considerations, and questions to guide future research. *Atmos. Res.*, **93**, 3–10, <https://doi.org/10.1016/j.atmosres.2008.09.015>.
- Martner, B. E., P. J. Neiman, and A. B. White, 2007: Collocated radar and radiosonde observations of a double-brightband melting layer in Northern California. *Mon. Wea. Rev.*, **135**, 2016–2024, <https://doi.org/10.1175/MWR3383.1>.
- Melnikov, V. M., and D. S. Zrnić, 2017: Observations of convective thermals with weather radar. *J. Atmos. Oceanic Technol.*, **34**, 1585–1590, <https://doi.org/10.1175/JTECH-D-17-0068.1>.
- , R. J. Doviak, D. S. Zrnić, and D. J. Stensrud, 2011: Mapping Bragg scatter with a polarimetric WSR-88D. *J. Atmos. Oceanic Technol.*, **28**, 1273–1285, <https://doi.org/10.1175/JTECH-D-10-05048.1>.
- , —, —, and —, 2013: Structures of Bragg scatter observed with the polarimetric WSR-88D. *J. Atmos. Oceanic Technol.*, **30**, 1253–1258, <https://doi.org/10.1175/JTECH-D-12-00210.1>.
- Nowotarski, C. J., P. M. Markowski, and Y. P. Richardson, 2011: The characteristics of numerically simulated supercell storms situated over statically stable boundary layers. *Mon. Wea. Rev.*, **139**, 3139–3162, <https://doi.org/10.1175/MWR-D-10-05087.1>.
- Park, H. S., A. V. Ryzhkov, D. S. Zrnić, and K.-E. Kim, 2009: The hydrometeor classification algorithm for the polarimetric WSR-88D: Description and application to an MCS. *Wea. Forecasting*, **24**, 730–748, <https://doi.org/10.1175/2008WAF2222205.1>.
- Pedregosa, F., and Coauthors, 2011: Scikit-learn: Machine learning in Python. *J. Mach. Learn. Res.*, **12**, 2825–2830.
- Penide, G., A. Protat, V. V. Kumar, and P. T. May, 2013: Comparison of two convective/stratiform precipitation classification techniques: Radar reflectivity texture versus drop size distribution-based approach. *J. Atmos. Oceanic Technol.*, **30**, 2788–2797, <https://doi.org/10.1175/JTECH-D-13-00019.1>.
- Poulos, G. S., and Coauthors, 2002: CASES-99: A comprehensive investigation of the stable nocturnal boundary layer. *Bull. Amer. Meteor. Soc.*, **83**, 555–581, [https://doi.org/10.1175/1520-0477\(2002\)083<0555:CACIOT>2.3.CO;2](https://doi.org/10.1175/1520-0477(2002)083<0555:CACIOT>2.3.CO;2).
- Pruppacher, H. R., and J. D. Klett, 2010: *Microphysics of Clouds and Precipitation*. Atmospheric and Oceanographic Sciences Library, Vol. 18, Springer, 954 pp.
- Qi, Y., J. Zhang, and P. Zhang, 2013: A real-time automated convective and stratiform precipitation segregation algorithm in native radar coordinates. *Quart. J. Roy. Meteor. Soc.*, **139**, 2233–2240, <https://doi.org/10.1002/qj.2095>.
- Ralph, F. M., 1995: Using radar-measured radial vertical velocities to distinguish precipitation scattering from clear-air scattering. *J. Atmos. Oceanic Technol.*, **12**, 257–267, [https://doi.org/10.1175/1520-0426\(1995\)012<0257:URMRVV>2.0.CO;2](https://doi.org/10.1175/1520-0426(1995)012<0257:URMRVV>2.0.CO;2).
- , P. J. Neiman, D. W. van de Kamp, and D. C. Law, 1995: Using spectral moment data from NOAA’s 404-MHz radar wind profilers to observe precipitation. *Bull. Amer. Meteor. Soc.*, **76**, 1717–1739, [https://doi.org/10.1175/1520-0477\(1995\)076<1717:USMDFN>2.0.CO;2](https://doi.org/10.1175/1520-0477(1995)076<1717:USMDFN>2.0.CO;2).
- , —, and D. Ruffieux, 1996: Precipitation identification from radar wind profiler spectral moment data: Vertical velocity histograms, velocity variance, and signal power–vertical velocity correlations. *J. Atmos. Oceanic Technol.*, **13**, 545–559, [https://doi.org/10.1175/1520-0426\(1996\)013<0545:PIFRWP>2.0.CO;2](https://doi.org/10.1175/1520-0426(1996)013<0545:PIFRWP>2.0.CO;2).
- Rasmussen, E. N., 2015: VORTEX-Southeast Program Overview. National Severe Storms Laboratory Rep., 36 pp.
- , and D. O. Blanchard, 1998: A baseline climatology of sounding-derived supercell and tornado forecast parameters. *Wea. Forecasting*, **13**, 1148–1164, [https://doi.org/10.1175/1520-0434\(1998\)013<1148:ABCOSD>2.0.CO;2](https://doi.org/10.1175/1520-0434(1998)013<1148:ABCOSD>2.0.CO;2).
- , and S. Koch, 2016: VORTEX-SE: Lessons learned and early results. *28th Conf. on Severe Local Storms*, Portland, Oregon, Amer. Meteor. Soc., 3.2, <https://ams.confex.com/ams/28SLS/webprogram/Paper301782.html>.
- Ravila, P., and J. Räsänen, 2004: New laser ceilometer using enhanced single lens optics. *Eighth Symp. on Integrated Observing and Assimilation Systems for Atmosphere, Oceans, and Land Surface*, Seattle, WA, Amer. Meteor. Soc., 4.11, https://ams.confex.com/ams/84Annual/techprogram/paper_68092.htm.
- Richardson, L. M., J. G. Cunningham, W. D. Zittel, R. R. Lee, R. L. Ice, V. M. Melnikov, N. P. Hoban, and J. G. Gebauer, 2017: Bragg scatter detection by the WSR-88D. Part I: Algorithm

- development. *J. Atmos. Oceanic Technol.*, **34**, 465–478, <https://doi.org/10.1175/JTECH-D-16-0030.1>.
- Rocadenbosch, F., G. Vázquez, and A. Comerón, 1998: Adaptive filter solution for processing lidar returns: Optical parameter estimation. *Appl. Opt.*, **37**, 7019–7034, <https://doi.org/10.1364/AO.37.007019>.
- , C. Soriano, A. Comerón, and J.-M. Baldasano, 1999: Lidar inversion of atmospheric backscatter and extinction-to-backscatter ratios by use of a Kalman filter. *Appl. Opt.*, **38**, 3175–3189, <https://doi.org/10.1364/AO.38.003175>.
- , R. L. Tanamachi, and S. J. Frasier, 2018: Atmospheric boundary-layer height tracking from S-band radar returns with an extended Kalman filter: Application to VORTEX-SE. *10th European Conf. on Radar Meteorology and Hydrology*, Wageningen, Netherlands, Wageningen University and Research, 11.12, http://projects.knmi.nl/erad2018/ERAD2018_abstract_028.pdf.
- Rose, T., S. Crewell, U. Löhnert, and C. Simmer, 2005: A network suitable microwave radiometer for operational monitoring of the cloudy atmosphere. *Atmos. Res.*, **75**, 183–200, <https://doi.org/10.1016/j.atmosres.2004.12.005>.
- Rosenfeld, D., E. Amitai, and D. B. Wolff, 1995: Classification of rain regimes by the three-dimensional properties of reflectivity fields. *J. Appl. Meteor.*, **34**, 198–211, [https://doi.org/10.1175/1520-0450\(1995\)034<0198:CORRBT>2.0.CO;2](https://doi.org/10.1175/1520-0450(1995)034<0198:CORRBT>2.0.CO;2).
- Ryzhkov, A., P. Zhang, H. Reeves, M. Kumjian, T. Tschallener, S. Trömel, and C. Simmer, 2016: Quasi-vertical profiles—A new way to look at polarimetric radar data. *J. Atmos. Oceanic Technol.*, **33**, 551–562, <https://doi.org/10.1175/JTECH-D-15-0020.1>.
- Sánchez-Diezma, R., I. Zawadzki, and D. Sempere-Torres, 2000: Identification of the bright band through the analysis of volumetric radar data. *J. Geophys. Res.*, **105**, 2225–2236, <https://doi.org/10.1029/1999JD900310>.
- Seibert, P., F. Beyrich, S.-E. Gryning, S. Joffre, A. Rasmussen, and P. Tiercer, 2000: Review and intercomparison of operational methods for the determination of the mixing height. *Atmos. Environ.*, **34**, 1001–1027, [https://doi.org/10.1016/S1352-2310\(99\)00349-0](https://doi.org/10.1016/S1352-2310(99)00349-0).
- Seidel, D. J., C. O. Ao, and K. Li, 2010: Estimating climatological planetary boundary layer heights from radiosonde observations: Comparison of methods and uncertainty analysis. *J. Geophys. Res.*, **115**, D16113, <https://doi.org/10.1029/2009JD013680>.
- Silverman, B. W., 1986: *Density Estimation for Statistics and Data Analysis*. CRC Press, 176 pp.
- Spuler, S. M., K. S. Repasky, B. Morley, D. Moen, M. Hayman, and A. R. Nehrir, 2015: Field-deployable diode-laser-based differential absorption lidar (DIAL) for profiling water vapor. *Atmos. Meas. Tech.*, **8**, 1073–1087, <https://doi.org/10.5194/amt-8-1073-2015>.
- Steiner, M., and J. A. Smith, 2002: Use of three-dimensional reflectivity structure for automated detection and removal of nonprecipitating echoes in radar data. *J. Atmos. Oceanic Technol.*, **19**, 673–686, [https://doi.org/10.1175/1520-0426\(2002\)019<0673:UOTDRS>2.0.CO;2](https://doi.org/10.1175/1520-0426(2002)019<0673:UOTDRS>2.0.CO;2).
- Stensrud, D. J., 2007: *Parameterization Schemes: Keys to Understanding Numerical Weather Prediction Models*. Cambridge University Press, 478 pp.
- Stull, R. B., 1988: *An Introduction to Boundary Layer Meteorology*. Kluwer Academic Publishers, 670 pp.
- Turner, D. D., 2016: CLAMPS boundary layer evolution observations during VORTEX-SE-2016. *28th Conf. on Severe Local Storms*, Portland, OR, Amer. Meteor. Soc., 3.7, <https://ams.confex.com/ams/28SL/webprogram/Paper300956.html>.
- , 2017: OU/NSSL CLAMPS AERI temperature and water vapor profile retrieval data. Version 1.0, NCAR/UCAR Earth Observing Laboratory, accessed 7 November 2017, <https://doi.org/10.5065/D69W0D7S>.
- , and U. Löhnert, 2014: Information content and uncertainties in thermodynamic profiles and liquid cloud properties retrieved from the ground-based Atmospheric Emitted Radiance Interferometer (AERI). *J. Climate Appl. Meteor.*, **53**, 752–771, <https://doi.org/10.1175/JAMC-D-13-0126.1>.
- van der Walt, S., J. L. Schönberger, J. Nunez-Iglesias, F. Boulogne, J. D. Warner, N. Yager, E. Goullart, and T. Yu, 2014: scikit-image: image processing in Python. *PeerJ*, **2**, e453, <https://doi.org/10.7717/peerj.453>.
- Wagner, T. J., P. M. Klein, and D. D. Turner, 2019: A new generation of ground-based mobile platforms for active and passive profiling of the boundary layer. *Bull. Amer. Meteor. Soc.*, **100**, 137–153, <https://doi.org/10.1175/BAMS-D-17-0165.1>.
- Waldinger, J., 2018: Improvements to the UMASS S-band FM-CW vertical wind profiling radar: System performance and data analysis. M.S.E.C.E. thesis, University of Massachusetts Amherst, 97 pp., https://scholarworks.umass.edu/masters_theses_2/674.
- , T. Hartley, W. Heberling, S. J. Frasier, and R. L. Tanamachi, 2017: S-band FMCW boundary layer profiler: System upgrades and results. *2017 IEEE Int. Geoscience and Remote Sensing Symp.*, Austin, Texas, IEEE, <https://doi.org/10.1109/IGARSS.2017.8128008>.
- Weckwerth, T. M., and Coauthors, 2004: An overview of the International H2O Project (IHOP_2002) and some preliminary highlights. *Bull. Amer. Meteor. Soc.*, **85**, 253–277, <https://doi.org/10.1175/BAMS-85-2-253>.
- Weisman, M. L., and J. B. Klemp, 1982: The dependence of numerically simulated convective storms on vertical wind shear and buoyancy. *Mon. Wea. Rev.*, **110**, 504–520, [https://doi.org/10.1175/1520-0493\(1982\)110<0504:TDonSC>2.0.CO;2](https://doi.org/10.1175/1520-0493(1982)110<0504:TDonSC>2.0.CO;2).
- White, A. B., C. J. Senff, and R. M. Banta, 1999: A comparison of mixing depths observed by ground-based wind profilers and an airborne lidar. *J. Atmos. Oceanic Technol.*, **16**, 584–590, [https://doi.org/10.1175/1520-0426\(1999\)016<0584:ACOMDO>2.0.CO;2](https://doi.org/10.1175/1520-0426(1999)016<0584:ACOMDO>2.0.CO;2).
- , D. J. Gottas, E. T. Strem, F. M. Ralph, and P. J. Neiman, 2002: An automated brightband height detection algorithm for use with Doppler radar spectral moments. *J. Atmos. Oceanic Technol.*, **19**, 687–697, [https://doi.org/10.1175/1520-0426\(2002\)019<0687:AABHDA>2.0.CO;2](https://doi.org/10.1175/1520-0426(2002)019<0687:AABHDA>2.0.CO;2).
- Wilczak, J. M., and Coauthors, 1995: Contamination of wind profiler data by migrating birds: Characteristics of corrupted data and potential solutions. *J. Atmos. Oceanic Technol.*, **12**, 449–467, [https://doi.org/10.1175/1520-0426\(1995\)012<0449:COWPDB>2.0.CO;2](https://doi.org/10.1175/1520-0426(1995)012<0449:COWPDB>2.0.CO;2).
- Wulfmeyer, V., and Coauthors, 2015: A review of the remote sensing of lower tropospheric thermodynamic profiles and its indispensable role for the understanding and the simulation of water and energy cycles. *Rev. Geophys.*, **53**, 819–895, <https://doi.org/10.1002/2014RG000476>.
- Zhang, J., S. Wang, and B. Clarke, 2004: WSR-88D reflectivity quality control using horizontal and vertical reflectivity structure. *11th Conf. on Aviation, Range, and Aerospace*, Hyannis, MA, Amer. Meteor. Soc., P5.4, https://ams.confex.com/ams/11aram22sls/techprogram/paper_81858.htm.
- , C. Langston, and K. Howard, 2008: Brightband identification based on vertical profiles of reflectivity from the WSR-88D. *J. Atmos. Oceanic Technol.*, **25**, 1859–1872, <https://doi.org/10.1175/2008JTECHA1039.1>.